JGR Space Physics

RESEARCH ARTICLE
10.1029/2021JA030078

Ultra-low Frequency Foreshock Waves and Ion Dynamics at Mars

R. Jarvinen[1,2], E. Kallio[1], and T. I. Pulkkinen[1,3]

[1]Department of Electronics and Nanoengineering, School of Electrical Engineering, Aalto University, Espoo, Finland, [2]Finnish Meteorological Institute, Helsinki, Finland, [3]Department of Climate and Space Sciences and Engineering, University of Michigan, Ann Arbor, MI, USA

Key Points:

- Two distinct foreshock ultra-low frequency (ULF) wave regions form in a global Mars-solar wind interaction hybrid simulation
- The ULF waves modulate ion precipitation and escape at Mars
- Ionospheric oxygen ion escape is enhanced by 60%–70% under radial interplanetary magnetic field

Supporting Information:

Supporting Information may be found in the online version of this article.

Correspondence to:

R. Jarvinen,
riku.jarvinen@aalto.fi

Citation:

Jarvinen, R., Kallio, E., & Pulkkinen, T. I. (2022). Ultra-low frequency foreshock waves and ion dynamics at Mars. *Journal of Geophysical Research: Space Physics*, *127*, e2021JA030078. https://doi.org/10.1029/2021JA030078

Received 26 OCT 2021
Accepted 4 APR 2022

Abstract We study the solar wind interaction with Mars in a global three-dimensional hybrid model. A well-developed, vast ion foreshock forms under a strongly flow-aligned interplanetary magnetic field (IMF) configuration but otherwise nominal solar wind and solar minimum photon flux conditions. Large-scale ultra-low frequency (ULF) waves are excited in the foreshock by backstreaming ions. The foreshock ULF waves constitute two distinct regions in the analyzed solar wind and IMF situation: the near region where the wave period is 71–83 s and the far region where the wave period is 25–28 s. The near foreshock region waves transmit downstream through the bow shock and affect dynamics of the solar wind and planetary ion populations. Especially, ion precipitation rate into the exobase and planetary ion escape rates fluctuate at the ULF wave period corresponding to the near foreshock region. The peak-to-peak amplitude of the modulation is few percent or less. Interestingly, ionospheric oxygen ion escape fluxes show more than two orders of magnitude local modulations in the heavy plume at the same period. Finally, the escape rates of the ionospheric oxygen ion populations are enhanced by 60–70% under flow-aligned IMF compared to nominal upstream conditions.

1. Introduction

Mars being the solar system's smallest planet with an atmosphere has a unique interaction with the solar wind. An induced planetary magnetosphere is formed when the solar wind interacts with an ionosphere of a globally unmagnetized planet like Mars and Venus (Lundin et al., 2007). The highly conductive dayside ionosphere causes the magnetized solar wind plasma flow to deviate around the planet. In this process, a magnetic barrier and an induced magnetosphere are formed. A bow shock is formed as the outermost boundary of a planetary plasma environment because the solar wind flow is typically supermagnetosonic. That is, the solar wind slows down and heats up when passing from the upstream to the downstream at the bow shock. The downstream region of turbulent, shocked plasma is called the magnetosheath. The magnetosheath is separated from the planetary plasma dominated region and the planetary wake by the induced magnetospheric boundary or the ionopause.

The compact size of Mars and its plasma environment mean that the finite Larmor (gyro) radius effects play an essential role in dynamics of escaping heavy planetary ions (Kallio & Jarvinen, 2012). Since an induced magnetosphere forms by the piling up of the interplanetary magnetic field (IMF) lines against an ionosphere, the solar wind flows close to the upper atmosphere and through the exosphere allowing direct acceleration of planetary ions by the electric fields associated with an induced magnetosphere and the solar wind (Brain et al., 2016). A portion of the accelerated planetary ions reach escape velocities from the Martian gravity well via several different escape channels or acceleration mechanisms and are lost to space (Dubinin et al., 2011). The planetary ion acceleration is driven by the solar wind interaction, but the total escape rate is affected also by the solar photon flux conditions (Nilsson et al., 2010; Ramstad et al., 2015).

Several of the escape channels are associated with steady-state acceleration mechanisms like the planetary ion pickup by the solar wind and the formation of the heavy ion plume (Dong et al., 2017; Futaana et al., 2017). In addition, also dynamical processes can affect planetary ion acceleration in induced magnetospheres (Dubinin et al., 2021; Jarvinen et al., 2020a; Luhmann et al., 1987; Lundin et al., 2011; Omidi et al., 2020). Especially, a foreshock is formed in the upstream region by backstreaming charged particle populations scattered near the bow shock (Brain et al., 2002; Eastwood et al., 2005; Mazelle et al., 2004). The ion foreshock forms in the region with a magnetic connection to the quasi-parallel bow shock where the angle between an outwards shock surface

normal and the magnetic field is small enough allowing ion scattering (<45°). The backstreaming particles are a source of free energy for plasma instability excitation, and, thus, the foreshock is rich in plasma structures and waves including prominent, large amplitude, magnetosonic ultra-low frequency (ULF) waves, which are observed at all solar system's terrestrial planets (Delva & Dubinin, 1998; Dubinin & Fraenz, 2016; Hoppe & Russell, 1982; Le et al., 2013). This way the foreshock "preprocesses" the solar wind before it encounters the quasi-parallel bow shock.

The orientation of the upstream IMF vector determines the location and extent of the foreshock. The IMF has two main polarities associated with the Parker spiral and different sides of the heliospheric current sheet: the toward (the Sun) sector ($B_x > 0$, $B_y < 0$) and the away (from the Sun) sector ($B_x < 0$, $B_y > 0$; Parker, 1958). The Parker spiral angle, the angle between the IMF vector and the assumed radial solar wind velocity vector, is typically about 57° (away sector) or 180°–57° = 123° (toward sector) at Mars (Slavin & Holzer, 1981). However, the IMF and the solar wind vary constantly and other conditions like closely flow-aligned IMF occur regularly (Liu et al., 2021; Luhmann et al., 1993). Strongly flow-aligned (radial) IMF conditions are interesting in the context of the current study since they result in the dayside foreshock and quasi-parallel bow shock ahead of the subsolar region (Fowler et al., 2019; Halekas et al., 2017). Conversely, strongly perpendicular IMF vector means that the bow shock is mostly quasi-perpendicular in the dayside of the planet and no proper subsolar foreshock forms under the solar minimum photon flux conditions. At solar maximum, upstream ULF waves are expected to be excited even under nominal IMF conditions (Parker spiral angle 57°) due an extended hydrogen exosphere and an enhanced photoionization compared to solar minimum (Bertucci et al., 2013; Chaffin et al., 2014; Delva & Dubinin, 1998; Romanelli et al., 2016; Yamauchi et al., 2015).

In addition to affecting the bow shock dynamics, the ULF foreshock waves transmit through the bow shock and travel in the magnetosheath and near the ionosphere and the exobase at Mars (Collinson et al., 2018). In the process, the ULF waves heat the dayside ionosphere and likely cause substantial planetary ion outflow (Fowler et al., 2018). The ULF waves are also likely responsible for other dynamical ion processes like the dispersed ion energization events observed at Mars (Collinson et al., 2018; Halekas et al., 2015). Further, charge exchange upstream of the bow shock is thought to be modulated by foreshock processes and these fluctuations are observed at low-altitudes as penetrating protons resulting from a secondary charge exchange (Fowler et al., 2019). All in all, the foreshock is a highly dynamical region and could play a major role in the acceleration of escaping planetary ions.

Here we present results on the foreshock ULF waves and their modulation of the plasma environment and ion escape and precipitation at Mars in a global hybrid simulation model. In the next section, we describe the most important features of the model to this study as well as the simulation run setup. Then we present our results on the overall structure of the Mars plasma environment and analyze the foreshock ULF waves and their effects near Mars in detail. Then we discuss the results and compare them to earlier theoretical and observations works. At the end, we summarize our findings.

2. Model

We use our highly parallelized global hybrid model to analyze the Mars-solar wind interaction (Jarvinen et al., 2018). In the model, ions are treated as macroscopic particle clouds (macroparticles) moving under the Lorentz force using a leap-frog algorithm. Each macroparticle represents a number of real physical particles described by the statistical weight of the macroparticle. Electrons form a charge-neutralizing and massless fluid. The magnetic field is advanced by Faraday's law and the total electric current density comes from Amperè's law. This way the ion dynamics (the ion charge density and the ion electric current density) are self-consistently coupled with the evolution of the magnetic field. Magnetized solar wind is injected in the simulation from the front ($+x$) wall and all walls allow free outflow of the plasma. The planetary obstacle (the inner boundary) to the solar wind flow is modeled as a superconducting sphere near the exobase, which the magnetic field cannot penetrate. Macroparticles entering the inner boundary are assumed precipitated and are removed from the simulation. The model equations and numerical schemes are the same as in our earlier studies with the exception of the electron pressure description. In this study, we use the scalar electron pressure term in Ohm's law, which assumes the ideal gas law in the adiabatic approximation with the polytropic index $\gamma = 2$ corresponding to two degrees of freedom perpendicular to the magnetic field. Further details of the algorithm can be found in Kallio and Janhunen (2002, 2003).

Four major Mars planetary ion populations are used in the simulation runs analyzed here. The populations are similar to in our earlier Mars works. The ionospheric atomic (O^+_{iono}) and molecular ($O^+_{2,iono}$) oxygen ions are emitted in the simulation at the model's inner boundary. The ionospheric emission has a cos(solar-zenith angle)

dependence on the dayside and a constant nightside emission of 10% of the noon emission. The ionospheric ions are emitted with a Maxwellian velocity distribution and the temperature of 2×10^4 K (Jarvinen et al., 2009). The emission rates of the ionospheric populations are selected so that they match in situ observations (Jarvinen et al., 2018). Moreover, photoions are produced from exospheric neutral coronae. This includes hot exospheric oxygen (O^+_{exo}) and hydrogen (H^+_{exo}) populations. The solar minimum photon flux ionization conditions are applied. Specifically, the neutral profiles are from "Run B (solar min, with exosphere)" of the "Intercomparison of Global Models and Measurements of the Martian Plasma Environment" International Space Science Institute (ISSI) team's second meeting (Brain, Barabash, et al., 2010; Egan et al., 2018; Jarvinen et al., 2018; Kallio et al., 2010; Modolo et al., 2016). The profiles are spherically symmetric and they are based on results by the Mars Thermosphere General Circulation Model (parameters Ls = 270 and $F_{10.7} = 34$; Bougher et al., 2008) and the Direct Simulation Monte Carlo dissociative recombination model for the Martian hot oxygen densities (Valeille et al., 2010).

The solar wind ions consist of proton (H^+_{sw}) and alpha (He^{++}_{sw}) populations; these refer to full populations including the incident solar wind core and the suprathermal/backstreaming foreshock beam, unless otherwise stated. The injection rates of all solar wind and planetary ion populations in the simulation domain are constant in time. The average numbers of macroparticles per grid cell are: Run 1: 175 (H^+_{sw}), 9 (He^{++}_{sw}), 19 (O^+_{iono}), 19 ($O^+_{2,iono}$), 25 (H^+_{exo}), and 29 (O^+_{exo}); Run 2: 177 (H^+_{sw}), 9 (He^{++}_{sw}), 15 (O^+_{iono}), 16 ($O^+_{2,iono}$), 7 (H^+_{exo}), and 9 (O^+_{exo}). However, note that the density, and, thus, the number of macroparticles per cell is highly variable for each population in the simulation domain.

Two three-dimensional simulation runs were performed for this study. Run 1 uses a highly flow-aligned (radial) IMF with the 6° spiral angle to allow the formation of an extensive, dayside ion foreshock in the simulation domain. Run 2 uses the nominal Parker Mars IMF with the spiral angle of 57° as a control case. Other than the IMF spiral angle, the runs have an identical setup corresponding to the nominal Mars upstream conditions (Slavin & Holzer, 1981). Note that we choose to change only one parameter, the IMF flow-aligned component, between the two runs. This allows us to distinguish its effect in the Mars-solar wind interaction in a reliable way. In practice, also other upstream conditions can covary with the spiral angle, and the average conditions can vary from solar minimum to solar maximum. To further simplify the situation, the Mars crustal magnetic anomalies and charge exchange and electron impact ionization of the exosphere are not included in the analyzed simulation runs.

Temporal scales include ion gyro periods of 20 s (H^+), 39 s (He^{++}), 316 s (O^+), and 631 s (O^+_2) in the undisturbed solar wind. Thermal gyro radii of the solar wind species are 123 km (H^+) and 229 km (He^{++}) and gyro radii of the heavy pickup ions are 2,258 km (O^+) and 4,517 km (O^+_2) in the undisturbed upstream solar wind in the radial IMF run.

The simulations were run for 1,000 s and the initialization and the formation of the foreshock took about 300 s. The analysis period was from t = 500…800 s, which includes about 4 periods of the near region ULF waves and 11 periods of the far region ULF waves.

See Table 1 for details of the numerical setup and the physical parameters of the simulation runs.

2.1. Coordinate System

The model uses a planet-centered coordinate system. The x axis is antiparallel to the incident, undisturbed solar wind flow, the y axis is aligned along the perpendicular IMF component to the undisturbed solar wind flow, and the z axis completes the right-handed coordinate system. Consequently, the z axis is along the convection electric field in the undisturbed solar wind. The hemisphere where the upstream solar wind convection electric field points away from the planet ($z > 0$) is termed the $+E_{sw}$ hemisphere and the $y < 0$ hemisphere is termed the foreshock hemisphere. The radius of Mars ($R_M = 3{,}390$ km) is used as the unit of length in the figures and the text.

Virtual spacecraft time series were recorded in three points (P1–P3) and ion velocity distributions in two points (P1 and P4):

$$\begin{aligned}
\text{P1} &= (x = 2.63,\ y = -0.57,\ z = -0.03)R_M && \text{(dayside foreshock / near region)}\\
\text{P2} &= (x = 1.23,\ y = -0.57,\ z = -0.03)R_M && \text{(subsolar magnetosheath)}\\
\text{P3} &= (x = -0.23,\ y = -0.03,\ z = 1.98)R_M && \text{(heavy ion plume)}\\
\text{P4} &= (x = -0.23,\ y = -4.43,\ z = -0.03)R_M && \text{(far region).}
\end{aligned}$$

Table 1
Global Hybrid Model Setup and Undisturbed Upstream Solar Wind (SW) and Interplanetary Magnetic Field (IMF) Conditions

Parameter	Value
Box size ($x \times y \times z$) [R_M]	$(-5\ldots10) \times (-10\ldots3) \times (-3\ldots3)$
Number of grid cells ($n_x \times n_y \times n_z$)	$300 \times 260 \times 120$
Grid cell size (Δx)	$(169.5\text{km})^3 = (R_M/20)^3$
Time step (Δt)	11.2 ms
SW bulk velocity vector [v_x, v_y, v_z]	[−430, 0, 0] km/s
H^+_{sw} temperature	6.1×10^4 K
He^{++}_{sw} temperature	21.35×10^4 K
H^+_{sw} density	3 cm^{-3}
He^{++}_{sw} density	0.12 cm^{-3}
Electron temperature	10^4 K
Run 1: IMF vector [B_x, B_y, B_z]	[−3.28, 0.344, 0] nT
Run 1: IMF spiral angle	6° (away sector)
Run 2: IMF vector [B_x, B_y, B_z]	[−1.797, 2.768, 0] nT
Run 2: IMF spiral angle	57° (away sector)
IMF magnitude	3.3 nT
Alfvén Mach number	11.1
Sonic Mach number	8.6
Magnetosonic Mach number	6.8
Plasma beta	1.7
Superconducting shell radius (R_η)	3,690 km = R_M + 300 km
Obstacle resistivity ($r < R_\eta$)	0
Plasma resistivity ($r \geq R_\eta$)	$8.92 \times 10^{-3} \times \mu_0 \Delta x^2/\Delta t$
Particle absorption radius	3,590 km = R_M + 200 km
H^+_{exo} photoion prod. rate	2.15×10^{24} s^{-1}
O^+_{exo} photoion prod. rate	2.67×10^{23} s^{-1}
O^+_{iono} ionospheric emis. rate	1.4×10^{25} s^{-1}
$O^+_{2,iono}$ ionospheric emis. rate	2.0×10^{25} s^{-1}
Ionospheric emis. radius	R_M + 400 km
Solar EUV photo rates	Solar minimum

See Figures 3b and 3c for the locations of the points.

3. Results

3.1. Large-Scale Structure

Figure 1 shows an overview of the solar wind proton kinetic, scalar temperature near Mars in both model runs. In the nominal run, the induced magnetosphere is well-formed and the IMF is piled up against the ionospheric obstacle forming the magnetic barrier. The induced magnetosphere is seen as increased temperature downstream of the bow shock compared to the undisturbed upstream region. In the radial IMF run, the boundaries of the induced magnetosphere are less well-defined due to the lack of a strong magnetic barrier.

The ion foreshock is seen in the $y < 0$ hemisphere as elevated upstream temperatures caused by the solar wind protons that are scattered upstream at the quasi-parallel bow shock. In the nominal run, the quasi-parallel bow shock is at larger than 90° solar-zenith angles near the back ($-x$) wall of the simulation domain and, thus, no proper foreshock forms close to the planet. In the radial IMF run, the quasi-parallel bow shock covers a large part of the $y < 0$ hemisphere on the $z = 0$ plane and the foreshock forms already in the near subsolar region. Top panels of Movie S1 in Supporting Information S1 show the dynamics of the temperature and the formation of the foreshock.

Figure 2 compares the magnetic field B_z component in both runs. B_z is the perpendicular component to the undisturbed solar wind velocity and IMF vectors. Consequently, any nonzero B_z values are associated with the Mars-solar wind interaction. Large-scale ULF waves are evident in the foreshock in the radial IMF run ($y < 0$ hemisphere). A minor B_z upstream disturbance is seen in the nominal run close to the back wall but no clear ULF waves occur. The propagation of the waves can be seen in the bottom panels of Movie S1 in Supporting Information S1.

Figure 3 gives an overview of the planetary O^+ density in the model. The exospheric photoions are seen as a spherical cloud reaching high-altitudes around the planet. Ionospheric ion emission is seen at lowest altitudes where the density is the highest. In the nominal run, the O^+ density is almost symmetric between the $y > 0$ and $y < 0$ hemispheres due to the small flow-aligned IMF component (B_x). That is, small B_x results in a small angle between the upstream solar wind velocity and the $E \times B$ drift velocity vectors. On the other hand, the radial IMF run has strong hemispheric asymmetries on the xy plane associated with highly perpendicular $E \times B$ drift to the solar wind velocity. The orientations of the upstream $E \times B$ velocity vectors are shown in Figures 3b and 3e. Both runs have strong hemispheric asymmetry in the direction of the convection electric field caused by the solar wind ion pickup. Movie S2 in Supporting Information S1 shows the dynamics of the O^+ ion density.

This concludes the comparative analysis of the two simulation runs. From here on we concentrate on the radial IMF run (Run 1) where a proper foreshock forms near Mars.

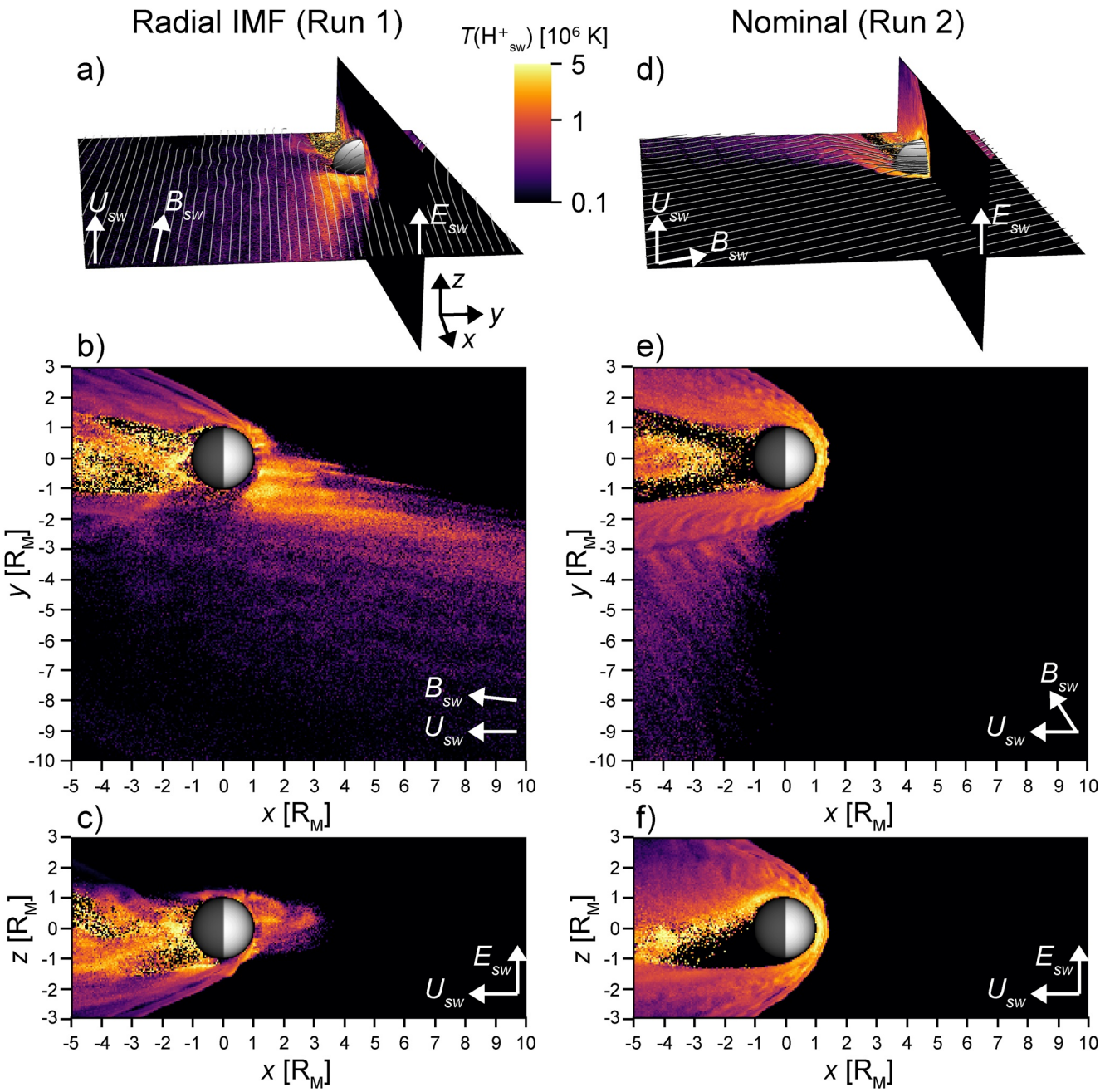

Figure 1. Overview of the Mars simulation run (a–c: Run 1, d–f: Run 2) snapshots at $t = 750$ s. The coloring gives the solar wind proton temperature at the xy ($z = 0$) and xz ($y = 0$) planes and the gray lines display the magnetic field lines. Three-dimensional field line tracing was started in the upstream region on the $z = 400$ km plane. The sphere shows the radius of Mars for context. The black and white arrows give the orientation of the coordinate axes and the undisturbed upstream solar wind bulk velocity $\left(\vec{U}_{\rm sw}\right)$, IMF $\left(\vec{B}_{\rm sw}\right)$ and convection electric field $\left(\vec{E}_{\rm sw}\right)$ vectors. See also Movie S1 in Supporting Information S1.

3.2. Foreshock and ULF Waves in the Radial IMF Run

Figure 4 displays spatial distribution of the B_z times series in the foreshock. Each insert shows $B_z(t)$ over a 500-s interval recorded in the simulation. The vertical axis has the height of 1 nT in all inserts and the axis is centered at the mean value. The full detailed version of the inserts is shown in Figure 5. The figures show that a range of different wave periods and amplitudes populate the foreshock. Largest absolute wave amplitudes occur around the lower left corner of Figures 4 and 5, where also the strongest ULF waves are seen in Figure 2 and Movie S1 in Supporting Information S1.

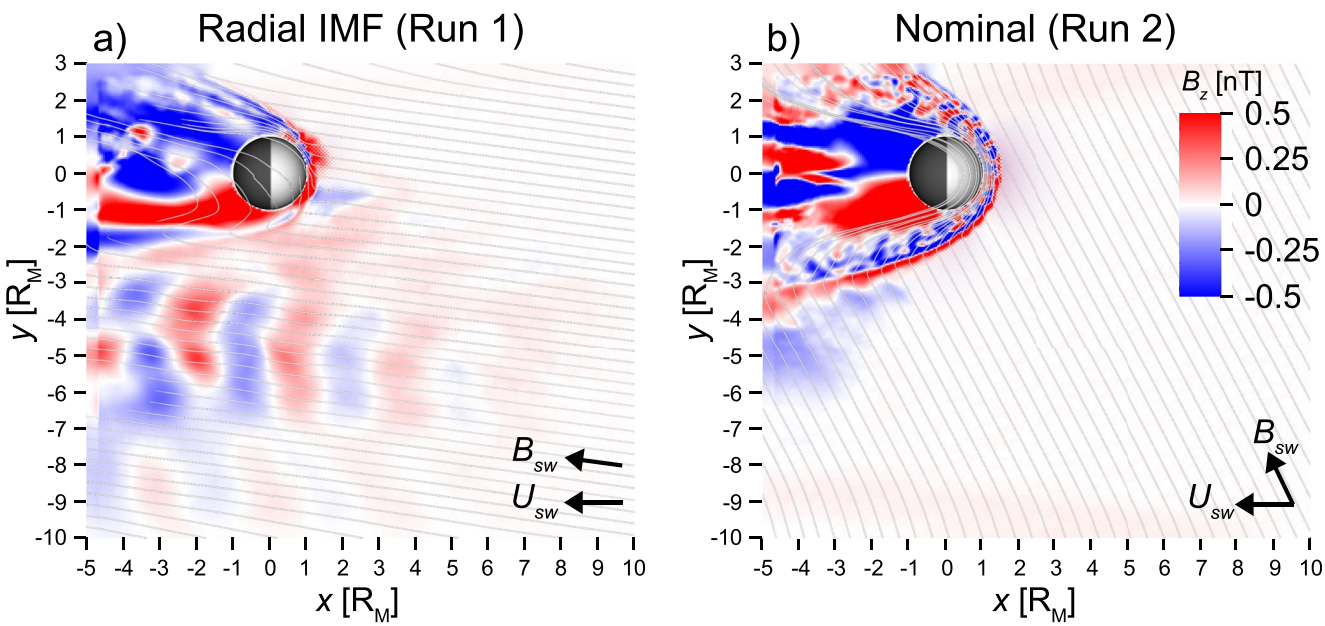

Figure 2. B_z component of the magnetic field (a: Run 1, b: Run 2) at the xy ($z = 0$) plane at $t = 750$ s. The gray lines display the magnetic field lines projected on the $z = 0$ plane. The figure format and the field lines are the same as in Figures 1b and 1e. See also Movie S1 in Supporting Information S1.

The $B_z(t)$ time series were Fourier transformed and they are shown in Figure 6. Then the period of the main ULF wave frequency was determined from the Fourier transformation (red circles in Figure 6), and the resulting periods are shown in Figure 7a. Two distinct wave regions are clearly identified. The lowest altitudes and the subsolar region show mostly longer wave periods between 71 and 83 s (the near region or the 83-s waves). Shorter periods of 25–28 s are found farther away from the planet where the wave amplitudes are the strongest (the far region or the 28-s waves). In addition, it can be seen in Figure 7b that the ULF waves have largely positive correlation between the plasma density and the magnetic field throughout the foreshock.

The foreshock waves are analyzed in more detail in Figures 8 and 9, where minimum variance analysis (MVA) and hodograms of the magnetic field are shown in the two regions. The locations where the hodograms are determined are denoted with dashed line in Figure 4. As can be seen in Figure 8, the waves in the near region are strongly elliptically polarized and propagate at an angle $\cos^{-1}\left(\hat{b}\cdot\hat{k}\right) = 89°$. The propagation is nearly perpendicular to the magnetic field in most of the near region. There is no fixed handedness of the wave polarization in the near region, but both left-handed to right-handed rotations are found.

Figure 9 shows the hodogram in the far region. It can be seen that the polarization here is closer to circular compared to the near region. The propagation angle is $\cos^{-1}\left(\hat{b}\cdot\hat{k}\right) = 48°$ in the analyzed point but it varies between 20° and 50° in the far region. The waves rotate in a left-handed sense with respect to the magnetic field in the simulation frame consistently throughout the far region.

3.3. Ion Velocity Distributions in the Foreshock

Figure 10 shows velocity distributions of the solar wind protons in the near and far foreshock regions at P1 and P4 (Figures 3b and 3c). The incident solar wind core is visible as a spherically symmetric population near the undisturbed upstream bulk velocity of [−430,0,0] km/s. The wide suprathermal (beam) population scattered at the bow shock is located away from the incident core antiparallel to the magnetic field. The suprathermal population is much wider and has a temperature of about one to two orders of magnitude higher than the core. Table 2 lists bulk properties of the core and suprathermal ion populations in Figure 10.

A major part of the near region suprathermal population is backstreaming ($v_x > 0$) and the population has a bulk velocity of [262, 0, −77] km/s in the simulation frame. In the far region, the major part of the suprathermal population is found between $v_x = -250\ldots0$ km/s and the population has a bulk velocity of [−53, −120, −25] km/s with only a small fraction backstreaming in the simulation frame. However, if the velocity distributions are

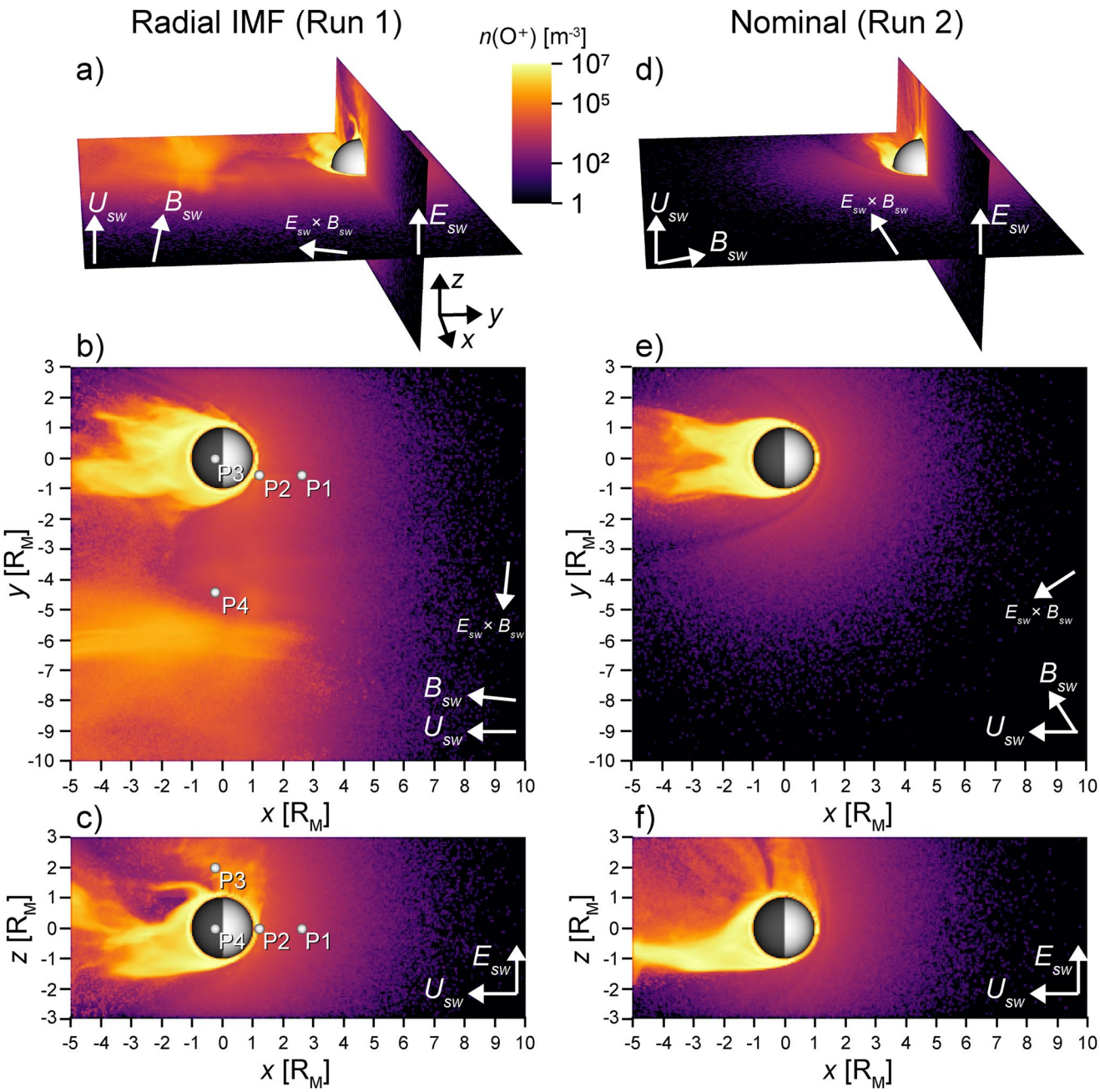

Figure 3. Overview of the O^+ density in Run 1 and Run 2 at $t = 750$ s. The figure is in the same format as Figure 1. The $\vec{E}_{sw} \times \vec{B}_{sw}$ arrows give the orientation of the undisturbed upstream $E \times B$ drift velocity. P1–P4 in panels b and c display the locations of points where virtual spacecraft time series and ion velocity distributions were determined. See also Movie S2 in Supporting Information S1.

transformed in the rest frame of the core, it can be seen that both the near and far region suprathermal populations are backstreaming toward the incident flow. The average density of the suprathermal beam varies from below 1% up to about 10% of the core in the foreshock.

3.4. Virtual Spacecraft Time Series

In order to analyze the foreshock plasma dynamics and the propagation of ULF waves near Mars in detail, time series of different quantities were determined in three points P1–P3 (Figures 3b and 3c).

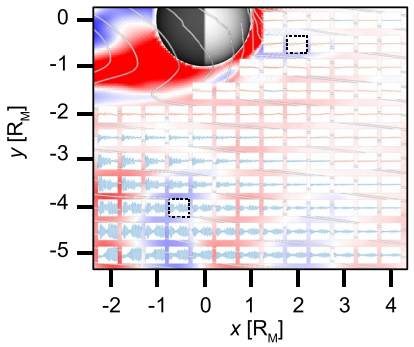

Figure 4. Spatial map of time series of the B_z component of the magnetic field in the foreshock in the radial IMF run at the xy ($z = 0$) plane. The background B_z figure with the magnetic field lines is the same as in Figure 2a. The inserts show $B_z(t)$ with time on the horizontal from 500 to 1,000 s and B_z on the vertical axis. The vertical axis is centered at the mean value of B_z in each point and the axis limits are mean(B_z) ± 0.5 nT. Both axes are linear. Each insert is centered around the point from where the time series was interpolated. Periods above 40 s are drawn in red and periods below 40 s in blue. The dashes lines show the locations where the minimum variance analysis is performed in Figures 8 and 9. See Figure 5 for a detailed version of the inserts.

Figure 11 shows the dayside foreshock point P1. The positively correlated fluctuations of the solar wind ion densities and the magnetic field at the ULF wave period of 83 s are evident. The exospheric H^+_{exo} density shows also weak ULF fluctuations while the exospheric O^+_{exo} density is dominated by statistical macroparticle noise.

Closer to the planet in the subsolar magnetosheath (P2) the ULF fluctuations become more pronounced than in the upstream foreshock as can be seen in Figure 12. Note that P1 and P2 are at the same line parallel to the x axis. Overall, the fluctuations have larger amplitude at P2 than at P1. Also the exospheric O^+_{exo} density shows strong fluctuations at the ULF period at P2. However, the maxima of oxygen densities are delayed compared to the maxima of the solar wind and exospheric H^+_{exo} densities and the magnetic field strength.

Figure 13 displays the point P3 in the heavy ion plume ($+E_{sw}$ hemisphere). Here the magnetic field does show as smooth, near sinusoidal ULF fluctuations as at P1 and P2, but the waveforms are more steepened or sawtooth type. The solar wind and exospheric ion densities do not fluctuate clearly in concert with the magnetic field. However, the plume has high ionospheric O^+_{iono} and $O^+_{2,iono}$ density and both of them show sharp increases in concert with the magnetic field wavefronts at near the ULF foreshock period. The maxima of O^+ densities occur before O^+_2 maxima, which can be understood as the two populations undergoing the same accelerating force associated with the ULF waves after being emitted from the inner boundary and the heavier population (O^+_2) lacking slightly behind.

Figure 14 analyzes the plume O^+_2 population in detail. It can be seen that the density spikes are associated with periodic time-energy spectrogram structures, where the velocity increases in concert with the density spikes.

Figure 5. Detailed time series of B_z in Figure 4. Panel titles give the coordinates of the points. The panels are organized in the rotated figure to increase the readability as follows: the x coordinate increases from the bottom of the page to the top and the y coordinate increases from right to left.

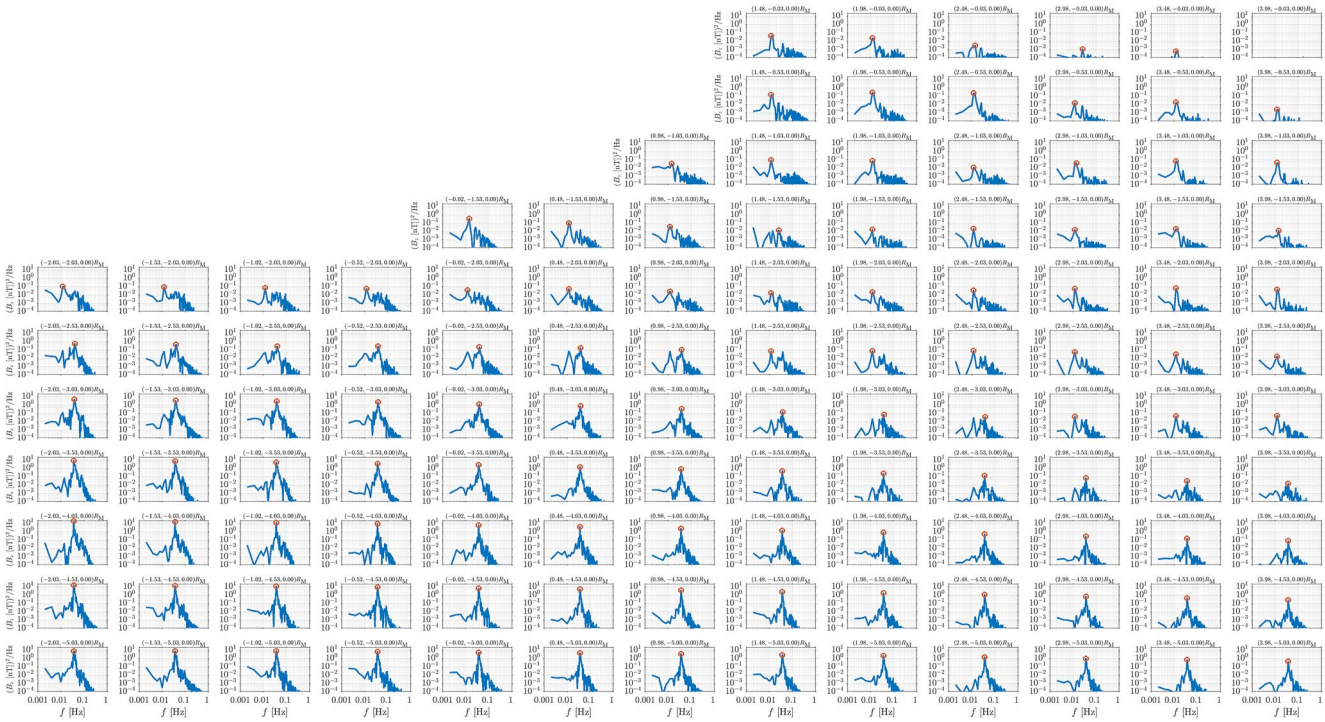

Figure 6. Power spectral density (PSD) of $B_z(t)$ in Figure 5. Red circles denote the maximum PSD, where periods above 100 s or power spectral densities less than 2×10^{-4} nT^2/Hz were ignored. A detrending with a running average over 100 s was applied before taking the fast Fourier transformation. The panels are organized in the same way as in Figure 5.

The velocity increase is directed along $v_y < 0$ and $v_z > 0$ direction, that is, toward the $+E_{sw}$ hemisphere and the foreshock hemisphere.

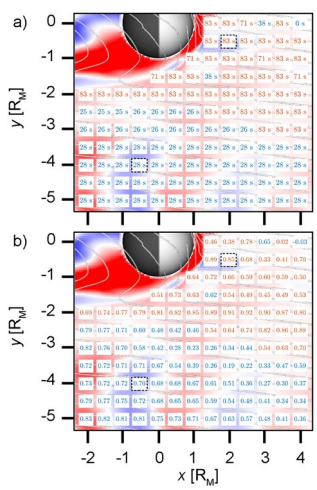

Figure 7. Spatial map of the foreshock ULF wave properties: (a) the maximum power spectral density periods of B_z determined in Figure 6, and (b) the Pearson correlation coefficient between the electron density and the magnitude of the magnetic field. Periods above 40 s are written in red and periods below 40 s in blue. The figure is in the same format as Figure 4.

3.5. Ion Escape and Precipitation

Figure 15 shows the time series of planetary ion escape rates from the simulation domain and the solar wind ion precipitation rates in the inner boundary in the radial IMF run. Table 3 lists time-averages of the escape and precipitation rates. The precipitation rates are determined by counting macroparticles that hit the inner boundary, which in the analyzed runs is close to the exobase, and are removed from the simulation. The escape rates are determined as the difference between the injection rate and the precipitation rate of a population.

It can be seen that the solar wind proton precipitation fluctuates close to the ULF period of 83 s. Moreover, also the ionospheric atomic and molecular oxygen ions and the exospheric photoion protons show fluctuations close to the period of 83 s. The peak-to-peak amplitude of the fluctuations is less than 5%. The solar wind alphas and the exospheric oxygen ions do not show such clear fluctuations.

4. Discussion

We show that a vast ion foreshock is created under radial IMF conditions (6° spiral angle) in a global Mars hybrid simulation. Under nominal IMF and solar minimum conditions (57° spiral angle) no proper foreshock forms and no large-scale ULF waves are excited near Mars (Figures 1 and 2). On the

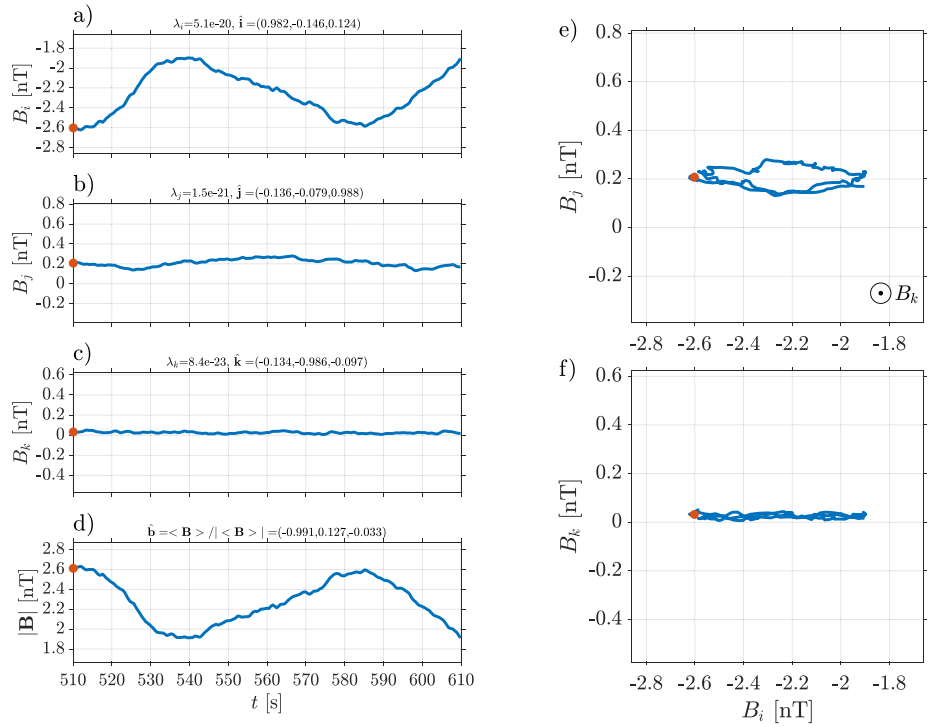

Figure 8. Minimum variance analysis (MVA) of the magnetic field in the near foreshock region. The point location is marked as dashed line around the insert in upper right quadrant in Figure 4a–4c. Left panels show the components of the magnetic field in the MVA coordinate system. In the left panel titles, λ_i, λ_j, and λ_k give the eigenvalues of the magnetic variance matrix and $\hat{i}$, $\hat{j}$, and $\hat{k}$ are the unit vectors of the maximum, intermediate, and minimum variance directions in the simulation coordinate system, respectively. The title of panel (d) gives the unit vector of the average magnetic field $(\hat{b})$ in the simulation coordinate system in the MVA analysis period. (e) The hodogram of the magnetic field on the plane of the maximum and intermediate variance directions. (f) The hodogram of the magnetic field on the plane of the maximum and minimum variance directions. The red dots denote the start of the time series.

other hand, the flow-aligned IMF results in a large portion of the bow shock being in the quasi-parallel regime allowing ion scattering and backstreaming already in the subsolar upstream region. In the foreshock, large-scale ULF waves are excited and form two distinct regions on the $z = 0$ plane (Figure 7): the near region and the far region. The wave periods of 71–83 s dominate the near region, whereas the periods of 25–28 s are found in the far region. As a comparison, the upstream ion gyro periods are from 20 s (H^+) to 631 s (O_2^+). The foreshock ULF wave period in the far region is just above the proton gyro period and below the alpha gyro period. In the near region, the ULF wave period is clearly above the proton and alpha gyro period but still below the oxygen gyro period. The period of the foreshock ULF waves based on earlier empirical model are in the range of 38–56 s for the upstream conditions in the radial IMF run (Hoppe & Russell, 1982; Le & Russell, 1996; Romanelli et al., 2020; Takahashi et al., 1984). These are in the range of the periods occurring in our model. It should be noted that such empirical formulae assume a single, fixed angle between the bow shock surface normal and the IMF, whereas in reality and in our global hybrid model the ion scattering at the quasi-parallel bow shock occurs over a range of angles.

The suprathermal foreshock ions are clearly identified in the ion velocity distributions and their properties differ substantially from the incident solar wind core population (Figure 10 and Table 2). It is evident that the suprathermal beam is backstreaming with respect to the core and has a much higher temperature perpendicular to the magnetic field compared to the parallel temperature. The backstreaming part of the velocity space reaches over 10% of total solar wind proton density in the subsolar foreshock near the boundary of the ion foreshock, whereas in the far region the backstreaming proton density is only few percent or below. There are only sporadic backstreaming solar wind alphas in the foreshock. Specifically, the suprathermal solar wind proton densities are 9% at P1 in the near region and 0.7% at P4 in the far region of the core. These are typical features of the terrestrial foreshock ion populations and the morphology of the suprathermal populations in Figure 10 qualitatively resemble

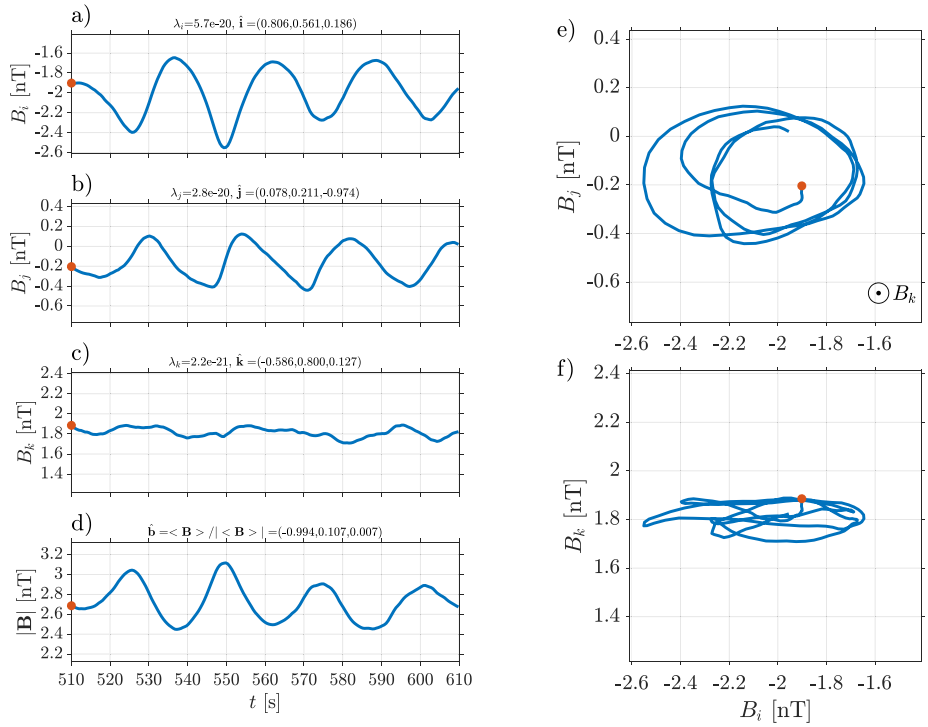

Figure 9. Minimum variance analysis (MVA) of the magnetic field in the far foreshock region. The point location is marked as dashed line around the insert in lower left quadrant in Figure 4. The figure is in the same format as Figure 8.

the field-aligned beam and intermediate ion distributions at Earth (e.g., reviews by Fuselier (1994), Eastwood et al. (2005), and Burgess et al. (2012), and references therein). The intermediate distributions are often associated with large-scale foreshock ULF waves (Fuselier et al., 1986; Hoppe et al., 1981; Paschmann et al., 1981).

Let us now investigate how strong are the ULF waves in different regions. The peak-to-peak relative magnitude of the ULF waves is about $dB/B = 0.3$ in the upstream subsolar foreshock (P1), and it increases up to $dB/B = 1.0$ in the subsolar magnetosheath (P2). This increase is due to the plasma and magnetic field compression at the bow shock and in the magnetic barrier as also seen in the observations (Collinson et al., 2018; Fowler et al., 2018). In the heavy ion plume, the magnitude is damped down to $dB/B = 0.2$ (P3) due to the waves propagating into plasma with increasing mass density but approximately constant magnetic pressure. The peak-to-peak relative magnitude of the solar wind proton (alpha) ULF fluctuation is about $dn/n = 0.6$ (1.3) at P1, which is compressed to $dn/n = 3.3$ (6.7) at P2. At P3, the magnitude is damped down to $dn/n < 0.2$ (0.5). The fluctuations are visible in the bulk density but also in the omnidirectional time-energy spectra. The absolute wave amplitudes are stronger in the far region than in the near region as can be seen in the time series in Figures 4 and 5, which is likely associated with backstreaming ion populations having longer time to interact with the incident solar wind flow via ion-ion instabilities and excite larger amplitude ULF waves (Gary, 1991).

Next, we estimate the wave length and the velocity of the ULF wave phases as follows (Jarvinen et al., 2020a). First, the magnetic field components are interpolated in a snapshot solution ($t = 560.4$ s) along a $4R_M$ long straight line in the wave propagation direction $\hat{k}$ centered at the near and far region points where the MVA was performed (Figure 4). Then the wave lengths (λ_w) are estimated from the interpolated B_i and B_j components of the MVA. Finally, the wave length and the period (τ_w) are combined to arrive at the phase speed $v_p = \lambda_w/\tau_w$. The wave length estimate in the near region is 3,800–5,800 km (22–34 grid cells) and 6,400–6,900 km (38–41 grid cells) in the far region. As a comparison, only oxygen species have the gyro radius of the same order of magnitude than the wave length of the foreshock ULF waves. The phase speed along $\hat{k}$ is estimate as 46–70 km/s in the near region and 230–246 km/s in the far region in the simulation frame. These are close to the solar wind bulk velocity projected along $\hat{k}$, which actually fluctuates above and below the phase speed due to variations caused by the foreshock and plasma thermal motion. Thus, the phase speed estimate is not conclusive to decide whether the waves are intrinsically left-handed or right-handed in the plasma frame.

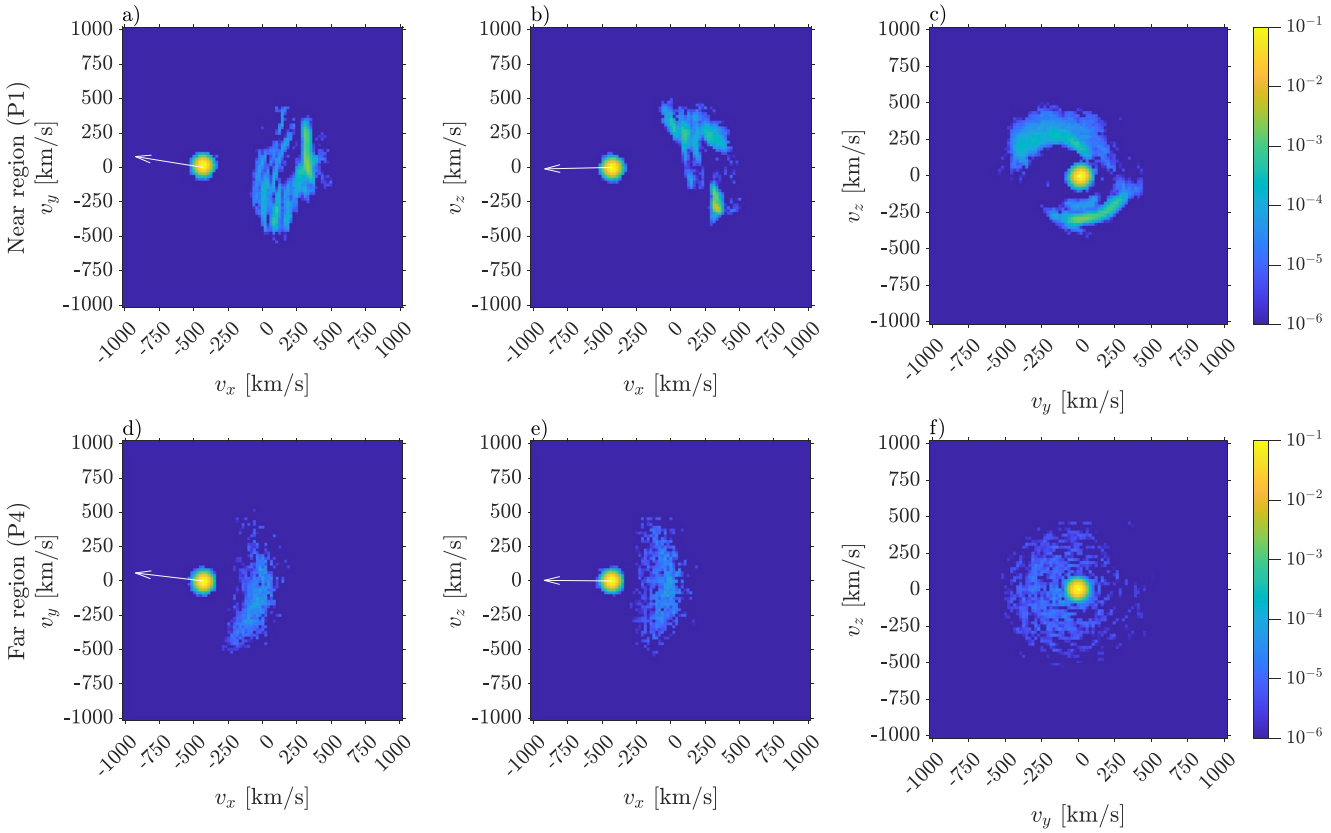

Figure 10. Solar wind proton (H^+_{sw}) velocity distributions in the near foreshock region at P1 (a–c) and in the far foreshock region at P4 (d–f) integrated over $t = 500…800$ s. The plots are projections of the whole three-dimensional distribution collapsed on the (v_x, v_y), (v_x, v_z), and (v_y, v_z) planes. The white arrows give the orientation of the average magnetic field vector projected on the planes over the same time interval. The coloring is the number of particles in each velocity bin divided by the total number of particles in the panel.

However, the correlation of the plasma density and the magnitude of the magnetic field is mostly strongly positive throughout the foreshock suggesting that the ULF waves are the fast magnetosonic mode in both foreshock regions (Figure 7b). In the near region, the propagation is nearly perpendicular the magnetic field and the polarization is highly elliptical with no clear handedness in the simulation frame due to fluctuations in the bulk velocity as discussed in the previous paragraph. On the other hand, the propagation angle of the waves is oblique with respect to the magnetic field (20–50°) and the polarization is consistently left-handed and circular in the simulation frame in the far region. This is what is expected from the right-handed ion-ion instability propagating upstream in the plasma frame, but convecting downstream with the solar wind flow in the simulation or spacecraft frame (Gary, 1991).

Table 2
Bulk Properties of the Incident Core and Suprathermal Foreshock H^+_{sw} *Populations Shown in Figure 10*

Region/population	Density(cm^{-3})	Temperature(10^4 K)	Bulk velocity(km/s)
Near (P1)			
/Core	2.76	6.1	[−428, 18, −1]
/Suprathermal	0.25	431.2	[262, 0, −77]
Far (P4)			
/Core	2.84	6.1	[−430, −3, 4]
/Suprathermal	0.02	282.2	[−53, −120, −25]

Note. The bulk velocity is given in the simulation frame.

As can be seen in Figure 14, the ion pickup is highly perpendicular to the undisturbed solar wind flow ($U_x \ll U_{yz}$) as expected under a strongly flow-aligned IMF. That is, the $E \times B$ drift is highly perpendicular to the flow (Figure 3) and the kinetic energy of pickup ions is much lower than under a nominal IMF (Jarvinen & Kallio, 2014). Further, large-scale planetary ion acceleration is modulated by the ULF waves as found also for Venus in our previous global hybrid modeling study (Jarvinen et al., 2020a). This can be seen in the dayside exospheric H^+_{exo} and O^+_{exo} photoion density fluctuations (Figures 11i and 12i, 12k). Further, the ionospheric O^+_{iono} and $O^+_{2,iono}$ densities show sharp modulations in concert with the arrival of the steepened ULF waves (Figures 13e and 13g) in the heavy ion plume. This creates the periodic structures, or "vortices," in the time-energy spectrograms of ionospheric oxygen ion populations (Figures 13 and 14). The velocity increase associated with

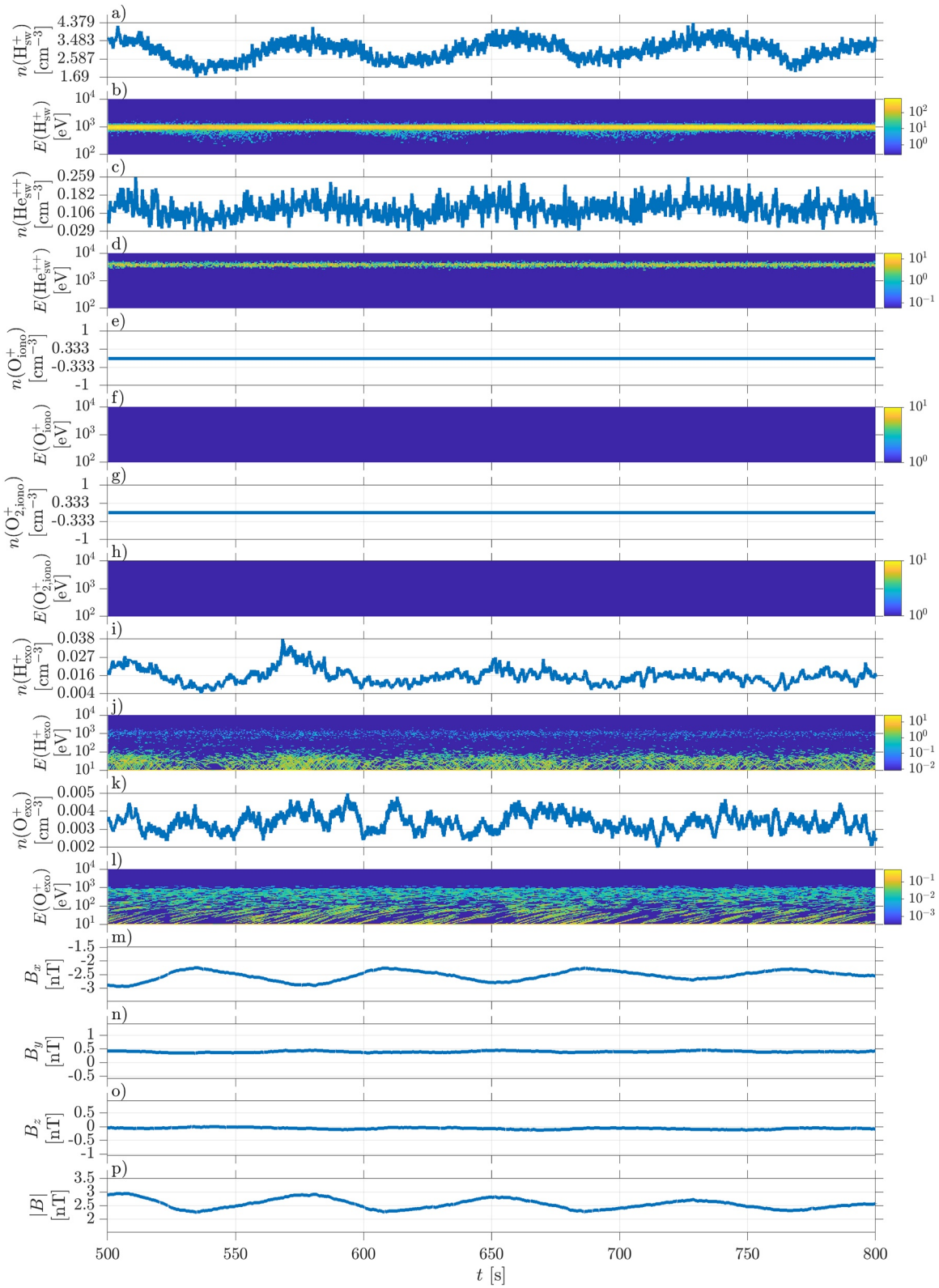
a)
b)
c)
d)
e)
f)
g)
h)
i)
j)
k)
l)
m)
n)
o)
p)
$n(H^+_{sw})$ [cm^{-3}]
$E(H^+_{sw})$ [eV]
$n(He^{++}_{sw})$ [cm^{-3}]
$E(He^{++}_{sw})$ [eV]
$n(O^+_{iono})$ [cm^{-3}]
$E(O^+_{iono})$ [eV]
$n(O^+_{2,iono})$ [cm^{-3}]
$E(O^+_{2,iono})$ [eV]
$n(H^+_{exo})$ [cm^{-3}]
$E(H^+_{exo})$ [eV]
$n(O^+_{exo})$ [cm^{-3}]
$E(O^+_{exo})$ [eV]
B_x [nT]
B_y [nT]
B_z [nT]
$|B|$ [nT]
500
550
600
650
700
750
800
t [s]

Figure 11.

the "vortices" is toward the $+E_{sw}$ hemisphere (increase in U_z) and the foreshock hemisphere (decrease in U_y). This ULF modulation of the heavy ion plume can be seen as periodically fluctuating density filaments and embedded oxygen ion bursts in the Movie S3 in Supporting Information S1. The bursts originate from low-altitudes near the inner boundary of the model and travel upwards resulting in the oxygen ion time-energy spectrogram vortices and density spikes. On the other hand, the periodic movement of the oxygen ion density filaments is associated with the wave-like behavior in the time-energy spectrogram between the vortices. This way, the ULF waves propagate in the heavy ion plume and locally detach oxygen ion bursts or clouds near the model's inner boundary. Recently, spacecraft observations of planetary ion heating by wave-particle interactions with the steepened magnetosonic ULF waves originating from the foreshock and extending from the dayside to the nightside and down to the exobase altitude was reported at Mars (Fowler et al., 2021).

Note that the ion density and velocity maxima do not exactly coincide with the magnetic field maxima in Figure 14. This is not completely unexpected as the ion motion is affected by the electric and magnetic fields (the Lorentz force) integrated along the ion trajectory rather than purely local fields. Point P3 is located 3,068 km above the model's inner boundary. This means that the escaping ionospheric oxygen ions had at least several tens of seconds of time to interact with the electric and magnetic fields associated with the ULF wavefronts before reaching P3 after emission from the inner boundary. At the lowest altitudes where the oxygen energies are below 10 eV the ions can stay one or few ULF wave periods within a single simulation cell. According to in situ observations by the Mars Atmosphere and Volatile EvolutioN (MAVEN) orbiter the wave lengths of the ULF waves compress from thousands of kilometers at the bow shock to hundreds of kilometers in the upper Martian ionosphere (Fowler et al., 2021). As a comparison, the simulation grid cell size is 169.5 km in this study, and a predetermined upwards emission of the ionospheric ions is used near the inner boundary rather than a more self-consistent description of the ionospheric photochemistry (e.g., Brecht et al., 2016; Ledvina et al., 2017; Modolo et al., 2016). Finite grid cell size results also in "reverse energy-time dispersed" signatures of H^+_{exo} and O^+_{exo} spectra at $\lesssim$100 eV energies in Figures 11–13. A dispersion signature is created when a single macroparticle is accelerated and gains energy within a grid cell. Even though our results demonstrate the connection between the foreshock ULF waves transmitted downstream and the modulation of the planetary heavy ion escape, more detailed simulations are needed to fully resolve the scales of the ULF wave—ionospheric ion interactions at the lowest altitudes.

Another important question is how the local ion escape is affected by the ULF waves in the heavy ion plume? The order of magnitude of the density variation is over 100 for O^+_2 and over 10 for O^+ at P3 (Figure 12), which can also be seen on the $+E_{sw}$ hemisphere in the upper *xz* and *yz* panels of Movies S2 and S3 in Supporting Information S1. Moreover, the local bulk escape flux varies more than two order of magnitude for these populations. Thus, the ULF waves modulate the heavy ion plume and planetary ion acceleration very strongly locally. Strong local variations (more than two orders of magnitude with respect to the mean value) in the heavy ion escape have also been observed by MAVEN and occur often in the $+E_{sw}$ hemisphere (Dubinin et al., 2021). It was proposed that is related to waves and instabilities.

Even though the local oxygen ion escape flux can increase more than two orders of magnitude in concert with the ULF wavefront, the integrated global escape rate is modulated only by few percents or less (Figure 15). This can be understood such that, even though the ULF waves modify the morphology of the heavy ion plume locally rather strongly, their modulation effect on the global ion escape is smoothed out by mixing of the different wave phases in the simulation domain. What is left in global scale is the average effect of the wave-particle interactions.

We speculate that the presence of crustal magnetic anomalies, which are not included in our current simulation runs, may play a role in the interaction between the ULF waves and the Martian ion escape. Specifically, is there a connection between the observed episodic bulk plasma escape bursts (Brain, Baker, et al., 2010; Fang

Figure 11. Virtual spacecraft time series of ions and magnetic field at P1 (dayside foreshock). Panels a–l show the density (n) and omnidirectional time-energy spectrogram (e) of different ion populations and panels m–p the magnetic field (b). The ion populations are the solar wind protons (H^+_{sw}), the solar wind alphas (He^{++}_{sw}), the ionospheric atomic oxygen (O^+_{iono}), the ionospheric molecular oxygen ($O^+_{2,iono}$), the exospheric hydrogen photoions (H^+_{exo}) and the exospheric oxygen photoions (O^+_{exo}). The coloring of the omnidirectional spectra were determined as $\sum_i w_i v_i/(4\pi\Delta V\Delta E)$ [(s^{-1} m^{-2} eV^{-1} sr^{-1})], where the summation i is over macroparticles in a grid cell (ΔV is the cell volume) averaged over 20 time steps, the energy range per bin is $[E, E + \Delta E]$, w_i is the statistical weight of a macroparticle, v_i is the speed of a macroparticle and the full solid angle is used to normalize the flux. Ninety nine logarithmically spaced energy bins were used in the range from 10 eV to 80 keV.

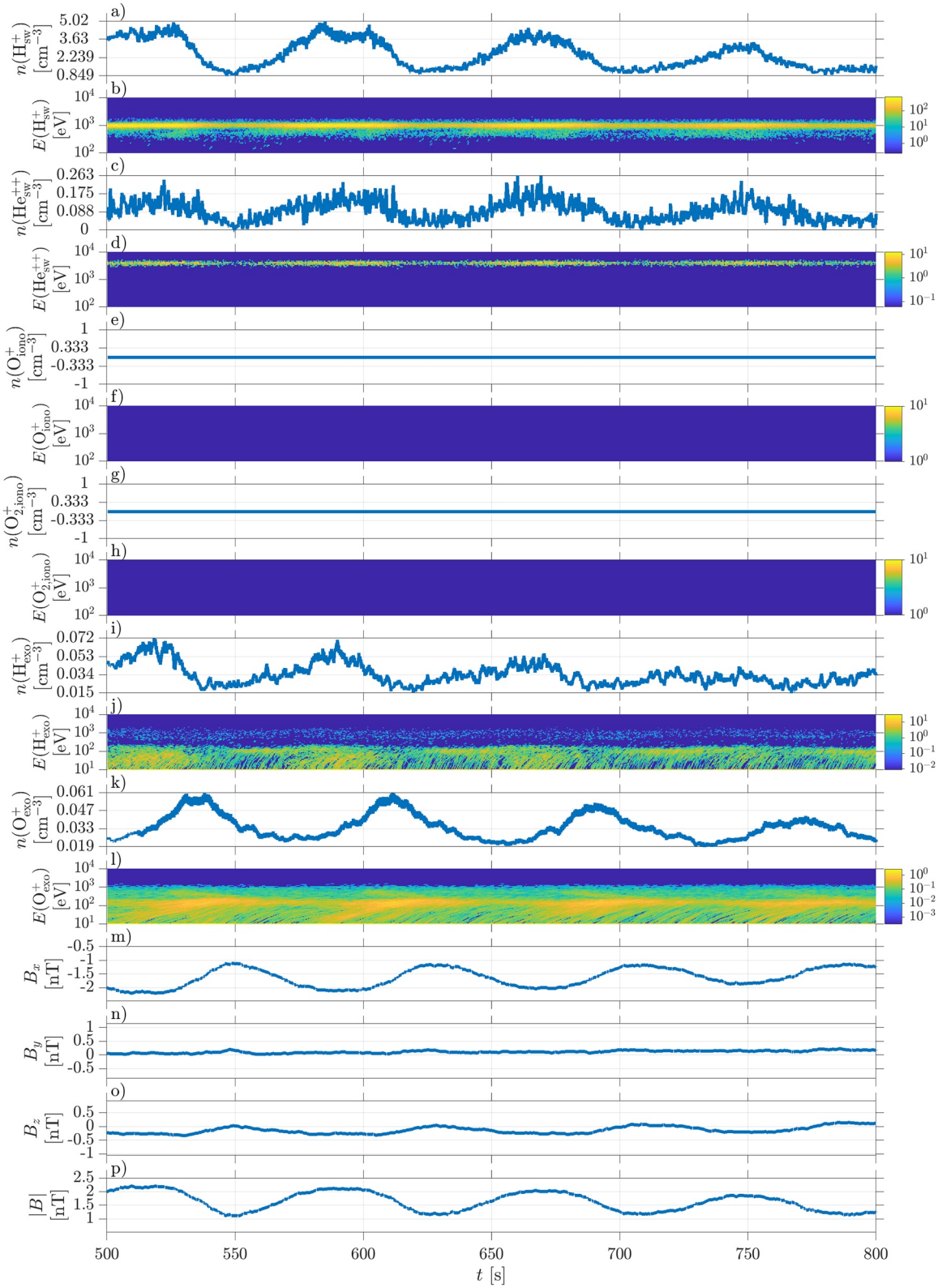

Figure 12. Virtual spacecraft time series of ions and magnetic field at P2 (subsolar magnetosheath). The figure is in the same format as Figure 11.

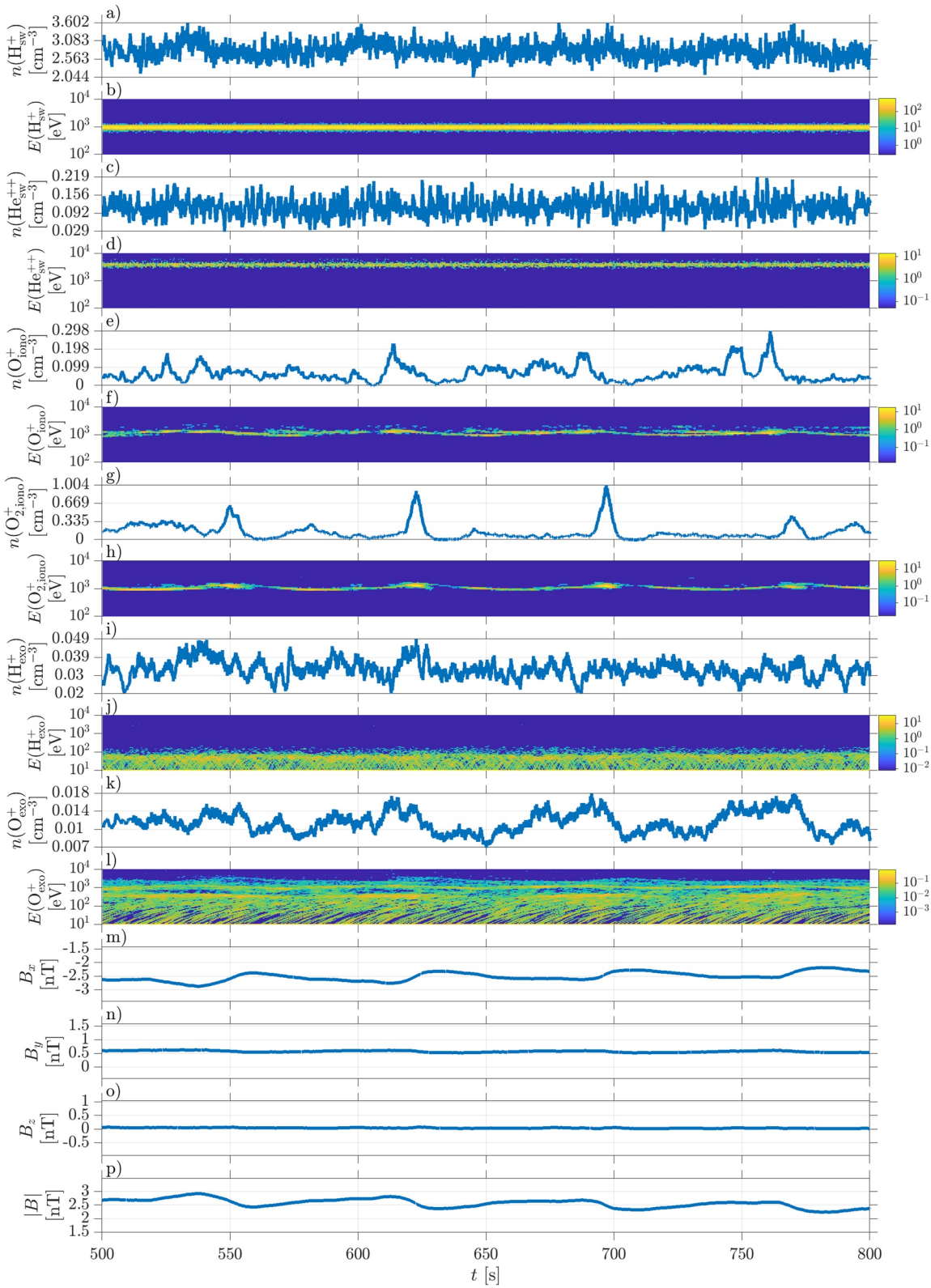

Figure 13. Virtual spacecraft time series of ions and magnetic field at P3 (heavy ion plume). The figure is in the same format as Figure 11.

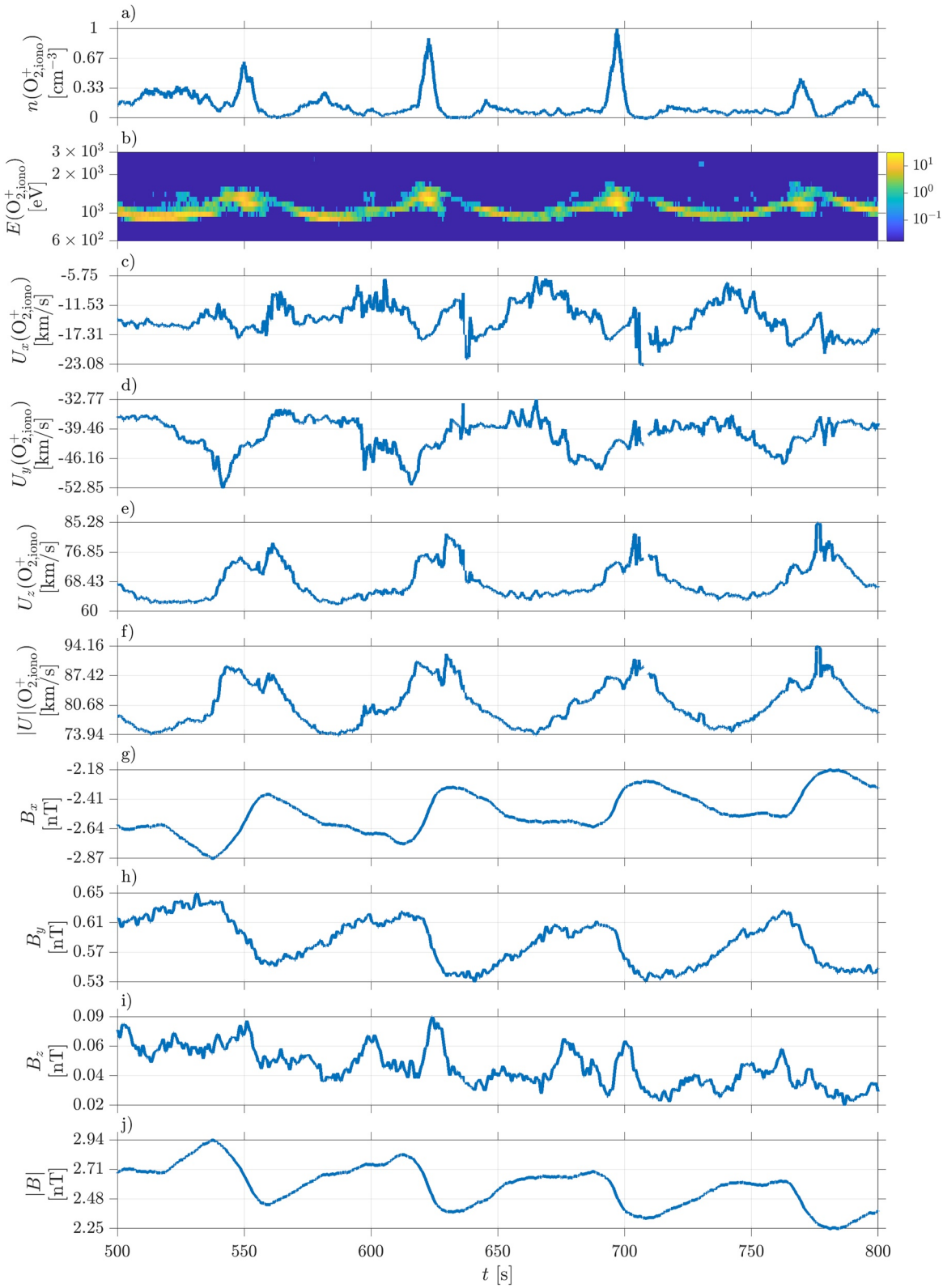

Figure 14. Virtual spacecraft time series of ionospheric O_2^+ ions at P3 (heavy ion plume). The topmost panels give the density (n) and the time-energy spectrogram (e) followed by the bulk velocity (U) and the magnetic field (b).

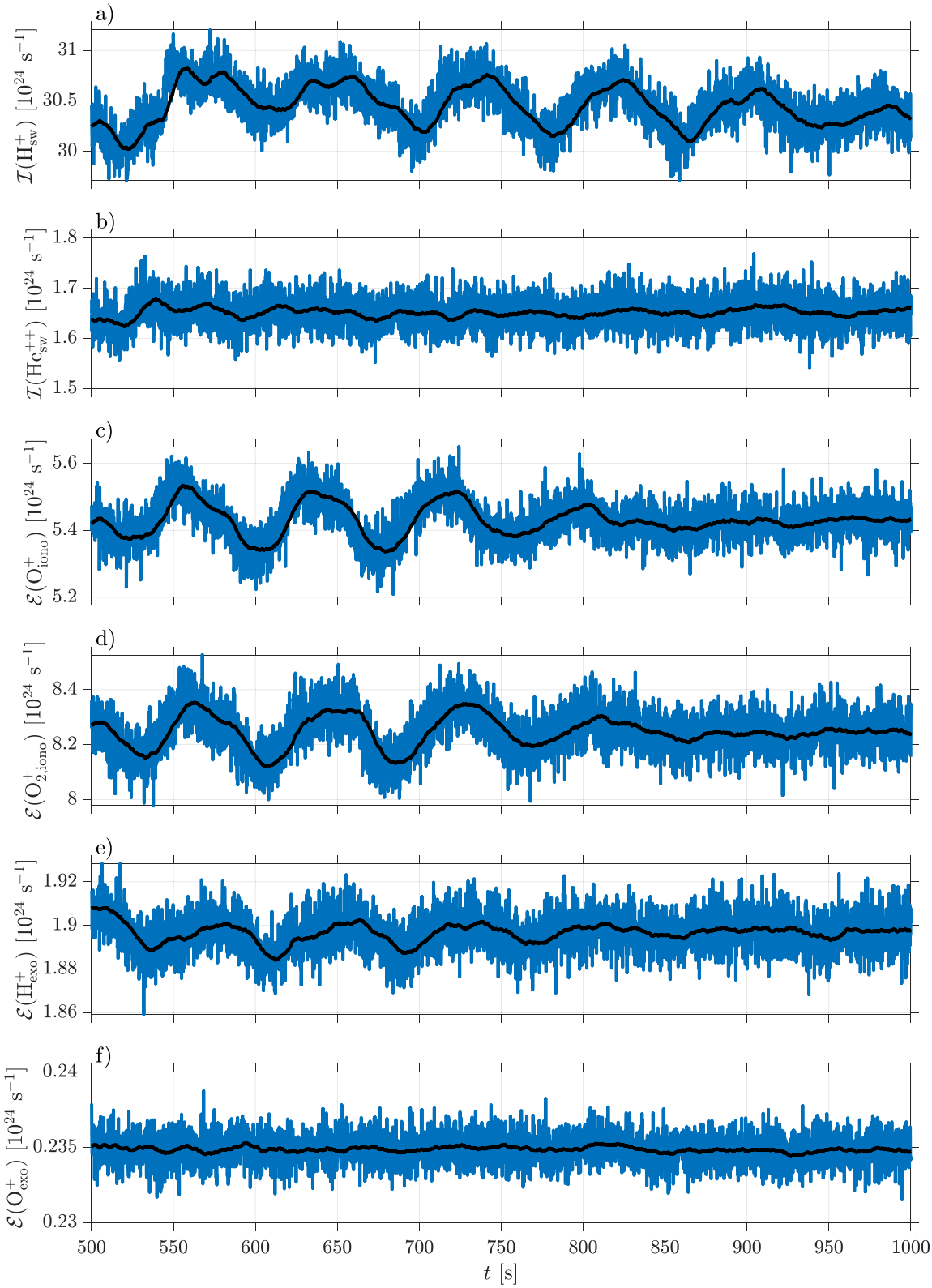

Figure 15. Time series global solar wind ion precipitation rates ($\mathcal{I}$) (a and b) and global planetary ion escape rates ($\mathcal{E}$)(c–f) in the radial IMF run. The black line gives the running average over 10 s.

Table 3
Global Temporal Average Ion Escape and Precipitation Rates and the Ratio of the Escape Rate to the Injection Rate of Planetary Ion Populations

Population	Precipitation rate (10^{24} s^{-1})	Escape rate (10^{24} s^{-1})	Escape/inject
Run 1			
H^+_{sw}	30.4	–	–
He^{++}_{sw}	1.6	–	–
O^+_{iono}	8.6	5.4	0.39
$O^+_{2,iono}$	11.8	8.2	0.41
H^+_{exo}	0.25	1.9	0.88
O^+_{exo}	0.03	0.23	0.88
Run 2			
H^+_{sw}	3.6	–	–
He^{++}_{sw}	0.24	–	–
O^+_{iono}	10.9	3.1	0.22
$O^+_{2,iono}$	15.0	5.0	0.25
H^+_{exo}	0.12	2.0	0.94
O^+_{exo}	0.05	0.22	0.82

Note. The sum of the escape rate and the precipitation rate equals to the injection rate in a stationary situation.

et al., 2017) and the foreshock ULF waves? The interplay of crustal magnetic fields and plasma waves in the Mars induced magnetosphere should be analyzed in future studies.

We emphasize that it is essential to take into account global context when analyzing in situ observation of planetary ion escape and, especially, waves and other spatiotemporal phenomena.

As a comparison, the foreshock ULF waves modulate the solar wind induced ion escape from Venus by 25% under nominal conditions in our earlier global hybrid modeling study (Jarvinen et al., 2020b). This is much stronger than a few percent at Mars found in this study. We attribute the difference to the denser solar wind and stronger IMF and, thus, stronger ULF waves at Venus. The nature of the ULF wave modulation of the planetary ion acceleration and plasma environment at Mars and Venus should be a topic for more detailed comparative studies using a range of upstream parameter cases at both planets.

Another difference between the foreshocks of Mars and Venus in a global hybrid simulation is the two ULF wave regions at Mars. The ULF modulation of the ion escape occurs at about the same period than the ULF waves in the near foreshock region (the 83-s waves). This is expected as the near region waves propagate toward the planet and the low-altitude, high-density regions where the initial planetary ion acceleration takes place. In the far region, the planetary ions have already reached high energies and their dynamics may not couple as efficiently with the ULF waves as in the near region. Also, the wave lengths in the far region are larger than the ion gyro radii of all ion species in the analyzed upstream condition case. However, the excitation and interplay of the ULF waves and the ion velocity distributions in the two foreshock regions should be a topic in a detailed study.

Table 3 lists the global escape rates of the planetary ion populations from the simulation domain, the precipitation rates of all ion populations to the inner boundary and the ratio of the escape rate to the injection rate per population for both runs. See Figure 15 (Figure S4 in Supporting Information S1) for time series of precipitation and escape rates in the radial IMF (nominal) run. The escape rates of ionospheric populations are enhanced by 74% (O^+_{iono}) and 64% ($O^+_{2,iono}$) in the radial IMF run compared to the nominal run. The increase in the ionospheric escape from an unmagnetized planet under a flow-aligned IMF has been associated with a change in the magnetic morphology of the induced magnetosphere and a disappearance of a well-developed magnetic barrier (Liu et al., 2009; Zhang et al., 2009). Moreover, even though the escape rates increases, the pickup ion energy becomes lower the more radial the IMF is due to the projection of the $E \times B$ velocity with respect to the solar wind flow (Jarvinen & Kallio, 2014). The gyroaveraged energy of a scatter-free pickup O^+ ion is 0.33 keV in the upstream solar wind in the radial IMF run and 22 keV in the nominal run, whereas the kinetic energy of an O^+ ion moving at the Mars escape velocity (5.03 km/s) is only 2.1 eV.

The exospheric photoion escape does not change considerably between our two runs. This is due to the fact that 80–90% of the created exospheric ions escape in both cases anyway, that is, the exospheric photoion escape is almost saturated or production limited (Ramstad et al., 2017). On the other hand, the ionospheric escape is more limited by acceleration processes or available momentum and energy and show a greater difference between the two runs. The obtained heavy ion escape rates are well within the estimates based on in situ spacecraft observations, which range from about the order of magnitude of 10^{24} to 10^{25} particles per second (see Dubinin et al., 2011; Jakosky et al., 2018, and references therein).

We find that the ULF waves also modulate the solar wind proton flux precipitating in the model's inner boundary near the exobase. The magnitude of this modulation is a few percent of the total precipitation flux (Figure 15). The alpha precipitation is not clearly affected by the ULF waves. This is likely due to longer He^{++} gyro radius (upstream: 229 km) compared to H^+ (upstream: 123 km). That is, the motion of alphas is more rigid compared to protons, and alphas can "jump" over the weak magnetic barrier whereas protons are more magnetized and can feel

the local ULF modulations as they are intensified in the region. The mean total solar wind H^+_{sw} (He^{++}_{sw}) precipitation rate under the radial IMF is 8.3 (6.8) times the value under the nominal IMF (Table 3). The increase is associated with the flow-aligned IMF opening a magnetic connection from the solar wind to the dayside inner boundary and in the same time the perpendicular IMF component is weak meaning that the pile up of the magnetic field and the creation of a proper magnetic barrier does not occur (Zhang et al., 2009). Together these allow the solar wind almost a direct entry to the inner boundary. The effect of the ULF wave modulation on the sputtering related escape at Mars (e.g., Martinez et al., 2020, and references therein) should be investigated in future studies.

5. Conclusions

We have analyzed the solar wind interaction with Mars in a global three-dimensional hybrid simulation. We find a well-developed ion foreshock under strongly radial IMF but otherwise nominal upstream solar wind conditions and solar minimum photon flux. We identify two distinct foreshock regions with fast magnetosonic ULF waves: the near region where the wave period is 71–83 s and the far region where the wave period is 25–28 s. The waves in the near region transmit downstream through the bow shock and affect dynamics of solar wind and planetary ions. Ion precipitation rates into the exobase and planetary ion escape rates show upto few percent peak-to-peak modulations at the ULF wave period corresponding to the near foreshock region. Ionospheric oxygen ion escape fluxes show more than two orders of magnitude local modulations in the heavy plume at the same period. Finally, the escape rates of the ionospheric oxygen ion populations are enhanced by 60–70% under radial IMF conditions compared to nominal upstream conditions.

Data Availability Statement

Global three-dimensional hybrid simulations were performed using the RHybrid simulation platform, which is available under an open-source license by the Finnish Meteorological Institute (https://github.com/fmihpc/rhybrid/). The simulation code version used in this study is archived (under doi: https://doi.org/10.5281/zenodo.6185399).

Acknowledgments
The work was supported by the Academy of Finland (Decision No. 310444). The authors thank the ISSI (International Space Science Institute) and ISSI-BJ (International Space Science Institute Beijing) team "Dayside Transient Phenomena and Their Impact on the Magnetosphere-Ionosphere" for discussions and suggestions. Figures 1–3 were created using the VisIt open-source visualization tool (Childs et al., 2012). We acknowledge the computational resources provided by the Aalto Science-IT project.

References

Bertucci, C., Romanelli, N., Chaufray, J. Y., Gomez, D., Mazelle, C., Delva, M., et al. (2013). Temporal variability of waves at the proton cyclotron frequency upstream from Mars: Implications for Mars distant hydrogen exosphere. *Geophysical Research Letters*, *40*, 3809–3813. https://doi.org/10.1002/grl.50709

Bougher, S. W., Blelly, P.-L., Combi, M., Fox, J. L., Mueller-Wodarg, I., Ridley, A., & Roble, R. G. (2008). Neutral upper atmosphere and ionosphere modeling. *Space Science Reviews*, *139*(1–4), 107–141. https://doi.org/10.1007/s11214-008-9401-9

Brain, D., Barabash, S., Boesswetter, A., Bougher, S., Brecht, S., Chanteur, G., et al. (2010). A comparison of global models for the solar wind interaction with Mars. *Icarus*, *206*, 139–151. https://doi.org/10.1016/j.icarus.2009.06.030

Brain, D. A., Bagenal, F., Acuña, M. H., Connerney, J. E. P., Crider, D. H., Mazelle, C., et al. (2002). Observations of low-frequency electromagnetic plasma waves upstream from the Martian shock. *Journal of Geophysical Research*, *107*(A6), 1076. https://doi.org/10.1029/2000JA000416

Brain, D. A., Bagenal, F., Ma, Y. J., Nilsson, H., & Stenberg Wieser, G. (2016). Atmospheric escape from unmagnetized bodies. *Journal of Geophysical Research: Planets*, *121*, 2364–2385. https://doi.org/10.1002/2016JE005162

Brain, D. A., Baker, A. H., Briggs, J., Eastwood, J. P., Halekas, J. S., & Phan, T.-D. (2010). Episodic detachment of Martian crustal magnetic fields leading to bulk atmospheric plasma escape. *Geophysical Research Letters*, *37*, L14108. https://doi.org/10.1029/2010GL043916

Brecht, S. H., Ledvina, S. A., & Bougher, S. W. (2016). Ionospheric loss from Mars as predicted by hybrid particle simulations. *Journal of Geophysical Research: Space Physics*, *121*, 10190–10208. https://doi.org/10.1002/2016JA022548

Burgess, D., Möbius, E., & Scholer, M. (2012). Ion acceleration at the earth's bow shock. *Space Science Reviews*, *173*, 5–47. https://doi.org/10.1007/s11214-012-9901-5

Chaffin, M. S., Chaufray, J.-Y., Stewart, I., Montmessin, F., Schneider, N. M., & Bertaux, J.-L. (2014). Unexpected variability of Martian hydrogen escape. *Geophysical Research Letters*, *41*, 314–320. https://doi.org/10.1002/2013GL058578

Childs, H., Brugger, E., Whitlock, B., Meredith, J., Ahern, S., Pugmire, D., et al. (2012). VisIt: An end-user tool for visualizing and analyzing very large data. In *High performance visualization—Enabling extreme-scale scientific insight* (pp. 357–372). CRC Press.

Collinson, G., Wilson, L. B., Omidi, N., Sibeck, D., Espley, J., Fowler, C. M., et al. (2018). Solar wind induced waves in the Skies of Mars: Ionospheric compression, energization, and escape resulting from the impact of ultralow frequency magnetosonic waves generated upstream of the Martian bow shock. *Journal of Geophysical Research: Space Physics*, *123*, 7241–7256. https://doi.org/10.1029/2018JA025414

Delva, M., & Dubinin, E. (1998). Upstream ULF fluctuations near Mars. *Journal of Geophysical Research*, *103*, 317–326. https://doi.org/10.1029/97JA02501

Dong, Y., Fang, X., Brain, D. A., McFadden, J. P., Halekas, J. S., Connerney, J. E. P., et al. (2017). Seasonal variability of Martian ion escape through the plume and tail from MAVEN observations. *Journal of Geophysical Research: Space Physics*, *122*, 4009–4022. https://doi.org/10.1002/2016JA023517

Dubinin, E., & Fraenz, M. (2016). Ultra-low-frequency waves at Venus and Mars. *American Geophysical Union Geophysical Monograph Series* (Vol. 216, pp. 343–364). Washington, DC: American Geophysical Union. https://doi.org/10.1002/9781119055006.ch20

Dubinin, E., Fraenz, M., Fedorov, A., Lundin, R., Edberg, N., Duru, F., & Vaisberg, O. (2011). Ion energization and escape on Mars and Venus. *Space Science Reviews*, *162*, 173–211. https://doi.org/10.1007/s11214-011-9831-7

Dubinin, E., Fraenz, M., Pätzold, M., Tellmann, S., Woch, J., McFadden, J., & Zelenyi, L. (2021). Bursty ion escape fluxes at Mars. *Journal of Geophysical Research: Space Physics*, *126*, e2020JA028920. https://doi.org/10.1029/2020JA028920

Eastwood, J. P., Lucek, E. A., Mazelle, C., Meziane, K., Narita, Y., Pickett, J., & Treumann, R. A. (2005). The foreshock. *Space Science Reviews*, *118*, 41–94. https://doi.org/10.1007/s11214-005-3824-3

Egan, H., Ma, Y., Dong, C., Modolo, R., Jarvinen, R., Bougher, S., et al. (2018). Comparison of global Martian plasma models in the context of MAVEN observations. *Journal of Geophysical Research: Space Physics*, *123*, 3714–3726. https://doi.org/10.1029/2017JA025068

Fang, X., Ma, Y., Masunaga, K., Dong, Y., Brain, D., Halekas, J., et al. (2017). The Mars crustal magnetic field control of plasma boundary locations and atmospheric loss: MHD prediction and comparison with MAVEN. *Journal of Geophysical Research: Space Physics*, *122*, 4117–4137. https://doi.org/10.1002/2016JA023509

Fowler, C. M., Andersson, L., Ergun, R. E., Harada, Y., Hara, T., Collinson, G., et al. (2018). MAVEN observations of solar wind-driven magnetosonic waves heating the Martian dayside ionosphere. *Journal of Geophysical Research: Space Physics*, *123*, 4129–4149. https://doi.org/10.1029/2018JA025208

Fowler, C. M., Halekas, J., Schwartz, S., Goodrich, K. A., Gruesbeck, J. R., & Benna, M. (2019). The modulation of solar wind hydrogen Deposition in the Martian atmosphere by foreshock phenomena. *Journal of Geophysical Research: Space Physics*, *124*, 7086–7097. https://doi.org/10.1029/2019JA026938

Fowler, C. M., Hanley, K. G., McFadden, J. P., Chaston, C. C., Bonnell, J. W., Halekas, J. S., et al. (2021). MAVEN observations of low frequency steepened magnetosonic waves and associated heating of the Martian nightside ionosphere. *Journal of Geophysical Research: Space Physics*, *126*, e2021JA029615. https://doi.org/10.1029/2021JA029615

Fuselier, S. A. (1994). *Suprathermal ions upstream and downstream from the Earth's bow shock*. *American Geophysical Union Geophysical Monograph Series* (Vol. 81, pp. 107–119). Washington, DC: American Geophysical Union. https://doi.org/10.1029/GM081p0107

Fuselier, S. A., Thomsen, M. F., Gosling, J. T., Bame, S. J., & Russell, C. T. (1986). Gyrating and intermediate ion distributions upstream from the earth's bow shock. *Journal of Geophysical Research*, *91*, 91–99. https://doi.org/10.1029/JA091iA01p00091

Futaana, Y., Stenberg Wieser, G., Barabash, S., & Luhmann, J. G. (2017). Solar wind interaction and impact on the Venus atmosphere. *Space Science Reviews*, *212*(3–4), 1453–1509. https://doi.org/10.1007/s11214-017-0362-8

Gary, S. P. (1991). Electromagnetic ion/ion instabilities and their consequences in space plasmas—A review. *Space Science Reviews*, *56*, 373–415. https://doi.org/10.1007/BF00196632

Halekas, J. S., McFadden, J. P., Connerney, J. E. P., Espley, J. R., Brain, D. A., Mitchell, D. L., et al. (2015). Time-dispersed ion signatures observed in the Martian magnetosphere by MAVEN. *Geophysical Research Letters*, *42*, 8910–8916. https://doi.org/10.1002/2015GL064781

Halekas, J. S., Ruhunusiri, S., Harada, Y., Collinson, G., Mitchell, D. L., Mazelle, C., et al. (2017). Structure, dynamics, and seasonal variability of the Mars-solar wind interaction: MAVEN solar wind ion analyzer in-flight performance and science results. *Journal of Geophysical Research: Space Physics*, *122*, 547–578. https://doi.org/10.1002/2016JA023167

Hoppe, M. M., & Russell, C. T. (1982). Particle acceleration at planetary bow shock waves. *Nature*, *295*, 41. https://doi.org/10.1038/295041a0

Hoppe, M. M., Russell, C. T., Frank, L. A., Eastman, T. E., & Greenstadt, E. W. (1981). Upstream hydromagnetic waves and their association with backstreaming ion populations - ISEE 1 and 2 observations. *Journal of Geophysical Research*, *86*, 4471–4492. https://doi.org/10.1029/JA086iA06p04471

Jakosky, B. M., Brain, D., Chaffin, M., Curry, S., Deighan, J., Grebowsky, J., et al. (2018). Loss of the Martian atmosphere to space: Present-day loss rates determined from MAVEN observations and integrated loss through time. *Icarus*, *315*, 146–157. https://doi.org/10.1016/j.icarus.2018.05.030

Jarvinen, R., Alho, M., Kallio, E., & Pulkkinen, T. I. (2020a). Oxygen ion escape from Venus is modulated by ultra-low frequency waves. *Geophysical Research Letters*, *47*, e2020GL087462. https://doi.org/10.1029/2020GL087462

Jarvinen, R., Alho, M., Kallio, E., & Pulkkinen, T. I. (2020b). Ultra-low-frequency waves in the ion foreshock of Mercury: A global hybrid modelling study. *Monthly Notices of the Royal Astronomical Society*, *491*(3), 4147–4161. https://doi.org/10.1093/mnras/stz3257

Jarvinen, R., Brain, D. A., Modolo, R., Fedorov, A., & Holmström, M. (2018). Oxygen ion energization at Mars: Comparison of MAVEN and Mars express observations to global hybrid simulation. *Journal of Geophysical Research: Spaces Physics*, *123*, 1678–1689. https://doi.org/10.1002/2017JA024884

Jarvinen, R., & Kallio, E. (2014). Energization of planetary pickup ions in the solar system. *Journal of Geophysical Research: Space Physics*, *119*, 219–236. https://doi.org/10.1002/2013JE004534

Jarvinen, R., Kallio, E., Janhunen, P., Barabash, S., Zhang, T. L., Pohjola, V., & Sillanpää, I. (2009). Oxygen ion escape from Venus in a global hybrid simulation: Role of the ionospheric O+ ions. *Annals of Geophysics*, *27*, 4333–4348.

Kallio, E., & Janhunen, P. (2002). Ion escape from Mars in a quasi-neutral hybrid model. *Journal of Geophysical Research*, *107*(A3), 1035. https://doi.org/10.1029/2001JA000090

Kallio, E., & Janhunen, P. (2003). Modelling the solar wind interaction with Mercury by a quasi-neutral hybrid model. *Annals of Geophysics*, *21*, 2133–2145.

Kallio, E., & Jarvinen, R. (2012). Kinetic effects on ion escape at Mars and Venus: Hybrid modeling studies. *Earth Planets and Space*, *64*, 157–163. https://doi.org/10.5047/eps.2011.08.014

Kallio, E., Liu, K., Jarvinen, R., Pohjola, V., & Janhunen, P. (2010). Oxygen ion escape at Mars in a hybrid model: High energy and low energy ions. *Icarus*, *206*, 152–163. https://doi.org/10.1016/j.icarus.2009.05.015

Le, G., Chi, P. J., Blanco-Cano, X., Boardsen, S., Slavin, J. A., Anderson, B. J., & Korth, H. (2013). Upstream ultra-low frequency waves in Mercury's foreshock region: MESSENGER magnetic field observations. *Journal of Geophysical Research: Space Physics*, *118*, 2809–2823. https://doi.org/10.1002/jgra.50342

Le, G., & Russell, C. T. (1996). Solar wind control of upstream wave frequency. *Journal of Geophysical Research*, *101*, 2571–2576. https://doi.org/10.1029/95JA03151

Ledvina, S. A., Brecht, S. H., Brain, D. A., & Jakosky, B. M. (2017). Ion escape rates from Mars: Results from hybrid simulations compared to MAVEN observations. *Journal of Geophysical Research: Space Physics*, *122*, 8391–8408. https://doi.org/10.1002/2016JA023521

Liu, D., Rong, Z., Gao, J., He, J., Klinger, L., Dunlop, M. W., et al. (2021). Statistical properties of solar wind upstream of Mars: MAVEN observations. *Acta Pathologica Japonica*, *911*(2), 113. https://doi.org/10.3847/1538-4357/abed50

Liu, K., Kallio, E., Jarvinen, R., Lammer, H., Lichtenegger, H. I. M., Kulikov, Y. N., et al. (2009). Hybrid simulations of the O^+ ion escape from Venus: Influence of the solar wind density and the IMF x component. *Advances in Space Research*, *43*, 1436–1441. https://doi.org/10.1016/j.asr.2009.01.005

Luhmann, J. G., Russell, C. T., Phillips, J. L., & Barnes, A. (1987). On the role of the quasi-parallel bow shock in ion pickup - a lesson from Venus? *Journal of Geophysical Research*, *92*, 2544–2550. https://doi.org/10.1029/JA092iA03p02544

Luhmann, J. G., Zhang, T., Petrinec, S. M., Russell, C. T., Gazis, P., & Barnes, A. (1993). Solar cycle 21 effects on the Interplanetary Magnetic Field and related parameters at 0.7 and 1.0 AU. *Journal of Geophysical Research*, *98*, 5559–5572. https://doi.org/10.1029/92JA02235

Lundin, R., Barabash, S., Dubinin, E., Winningham, D., & Yamauchi, M. (2011). Low-altitude acceleration of ionospheric ions at Mars. *Geophysical Research Letters*, *38*, L08108. https://doi.org/10.1029/2011GL047064

Lundin, R., Lammer, H., & Ribas, I. (2007). Planetary magnetic fields and solar forcing: Implications for atmospheric evolution. *Space Science Reviews*, *129*, 245–278. https://doi.org/10.1007/s11214-007-9176-4

Martinez, A., Modolo, R., Leblanc, F., Chaufray, J. Y., Witasse, O., Romanelli, N., et al. (2020). Influence of the solar wind dynamic pressure on the ion precipitation: MAVEN observations and simulation results. *Journal of Geophysical Research*, *125*, e2020JA028183. https://doi.org/10.1029/2020JA028183

Mazelle, C., Winterhalter, D., Sauer, K., Trotignon, J. G., Acuña, M. H., Baumgärtel, K., et al. (2004). Bow shock and upstream phenomena at Mars. *Space Science Reviews*, *111*(1), 115–181. https://doi.org/10.1023/B:SPAC.0000032717.98679.d0

Modolo, R., Hess, S., Mancini, M., Leblanc, F., Chaufray, J.-Y., Brain, D., et al. (2016). Mars-solar wind interaction: LatHyS, an improved parallel 3-D multispecies hybrid model. *Journal of Geophysical Research: Space Physics*, *121*, 6378–6399. https://doi.org/10.1002/2015JA022324

Nilsson, H., Carlsson, E., Brain, D. A., Yamauchi, M., Holmström, M., Barabash, S., et al. (2010). Ion escape from Mars as a function of solar wind conditions: A statistical study. *Icarus*, *206*(1), 40–49. https://doi.org/10.1016/j.icarus.2009.03.006

Omidi, N., Collinson, G., & Sibeck, D. (2020). Foreshock bubbles at Venus: Hybrid simulations and VEX observations. *Journal of Geophysical Research: Space Physics*, *125*, e2020JA27056. https://doi.org/10.1029/2019JA027056

Parker, E. N. (1958). Dynamics of the interplanetary gas and magnetic fields. *Acta Pathologica Japonica*, *128*, 664. https://doi.org/10.1086/146579

Paschmann, G., Sckopke, N., Papamastorakis, I., Asbridge, J. R., Bame, S. J., & Gosling, J. T. (1981). Characteristics of reflected and diffuse ions upstream from the earth's bow shock. *Journal of Geophysical Research*, *86*, 4355–4364. https://doi.org/10.1029/JA086iA06p04355

Ramstad, R., Barabash, S., Futaana, Y., Nilsson, H., & Holmström, M. (2017). Global Mars-solar wind coupling and ion escape. *Journal of Geophysical Research: Space Physics*, *122*, 8051–8062. https://doi.org/10.1002/2017JA024306

Ramstad, R., Barabash, S., Futaana, Y., Nilsson, H., Wang, X.-D., & Holmström, M. (2015). The Martian atmospheric ion escape rate dependence on solar wind and solar EUV conditions: 1. Seven years of Mars Express observations. *Journal of Geophysical Research: Space Physics*, *120*, 1298–1309. https://doi.org/10.1002/2015JE004816

Romanelli, N., DiBraccio, G., Gershman, D., Le, G., Mazelle, C., Meziane, K., et al. (2020). Upstream ultra-low frequency waves observed by MESSENGER's Magnetometer: Implications for particle acceleration at Mercury's bow shock. *Geophysical Research Letters*, *47*, e2020GL087350. https://doi.org/10.1029/2020GL087350

Romanelli, N., Mazelle, C., Chaufray, J. Y., Meziane, K., Shan, L., Ruhunusiri, S., et al. (2016). Proton cyclotron waves occurrence rate upstream from Mars observed by MAVEN: Associated variability of the Martian upper atmosphere. *Journal of Geophysical Research: Space Physics*, *121*, 11113–11128. https://doi.org/10.1002/2016JA023270

Slavin, J. A., & Holzer, R. E. (1981). Solar wind flow about the terrestrial planets. I—Modeling bow shock position and shape. *Journal of Geophysical Research*, *86*, 11401–11418. https://doi.org/10.1029/JA086iA13p11401

Takahashi, K., McPherron, R. L., & Terasawa, T. (1984). Dependence of the spectrum of Pc 3-4 pulsations on the interplanetary magnetic field. *Journal of Geophysical Research*, *89*, 2770–2780. https://doi.org/10.1029/JA089iA05p02770

Valeille, A., Combi, M. R., Tenishev, V., Bougher, S. W., & Nagy, A. F. (2010). A study of suprathermal oxygen atoms in Mars upper thermosphere and exosphere over the range of limiting conditions. *Icarus*, *206*(1), 18–27. https://doi.org/10.1016/j.icarus.2008.08.018

Yamauchi, M., Hara, T., Lundin, R., Dubinin, E., Fedorov, A., Sauvaud, J. A., et al. (2015). Seasonal variation of Martian pick-up ions: Evidence of breathing exosphere. *Planetary and Space Science*, *119*, 54–61. https://doi.org/10.1016/j.pss.2015.09.013

Zhang, T. L., Du, J., Ma, Y. J., Lammer, H., Baumjohann, W., Wang, C., & Russell, C. T. (2009). Disappearing induced magnetosphere at Venus: Implications for close-in exoplanets. *Geophysical Research Letters*, *36*, L20203. https://doi.org/10.1029/2009GL040515